BNL-227548-2025-TECH

EIC-ADD-TN-115

Advancements in Accelerator Physics and System Developments for the EIC

A. Blednykh

October 2024

Electron-Ion Collider Project

Brookhaven National Laboratory

U.S. Department of Energy

USDOE Office of Science (SC), Nuclear Physics (NP)

Notice: This technical note has been authored by employees of Brookhaven Science Associates, LLC under Contract No.DE-SC0012704 with the U.S. Department of Energy. The publisher by accepting the technical note for publication acknowledges that the United States Government retains a non-exclusive, paid-up, irrevocable, world-wide license to publish or reproduce the published form of this technical note, or allow others to do so, for United States Government purposes.

DISCLAIMER

This report was prepared as an account of work sponsored by an agency of the United States Government. Neither the United States Government nor any agency thereof, nor any of their employees, nor any of their contractors, subcontractors, or their employees, makes any warranty, express or implied, or assumes any legal liability or responsibility for the accuracy, completeness, or any third party's use or the results of such use of any information, apparatus, product, or process disclosed, or represents that its use would not infringe privately owned rights. Reference herein to any specific commercial product, process, or service by trade name, trademark, manufacturer, or otherwise, does not necessarily constitute or imply its endorsement, recommendation, or favoring by the United States Government or any agency thereof or its contractors or subcontractors. The views and opinions of authors expressed herein do not necessarily state or reflect those of the United States Government or any agency thereof.

Advancements in Accelerator Physics and System Developments for the EIC

A. Blednykh, P. Baxevanis, W. Bergan, J. S. Berg, J. Biswas,
M. Blaskiewicz, X. Gu, Y.-K. Kan, Y. Luo, D. Marx,
C. Montag, H. Oh, B. Podobedov, V. Ptitsyn, V. Ranjbar, V. Shmakova,
S. Tepikian, N. Tsoupas, S. Verdú-Andrés, E. Wang, G. Wang, Q. Wu, D. Xu
Brookhaven National Laboratory, Upton, New York 11973, USA
Y. Cai, Y. Nosochkov,
SLAC, Menlo Park, CA 94025, USA
T. Satogata,
Jefferson Lab, Newport News, VA 23606, USA

October 2024

1 Introduction

The development and enhancement of the Electron-Ion Collider (EIC) are founded on extensive research and development efforts aimed at achieving rigorous performance goals. This document outlines the crucial research and development (R&D) efforts that underpin the various systems and components of the EIC, including the polarized electron source and linear accelerator (linac) systems. Achieving the collider's operational benchmarks relies on meticulously enhancing these components to optimize performance.

This report delves into key accomplishments across several focus areas, highlighting advancements in electron source polarization, bunch charge capabilities, linac acceleration strategies, impedance management, collective effects, beam cooling technologies, beam dynamics, stability, transfer lines, and spin dynamics. By showcasing these improvements, we aim to provide a comprehensive overview of the current state of EIC development, emphasizing the collaborative efforts that drive innovation in accelerator physics and related technologies.

2 Electron Injector

2.1 Polarized electron source

The polarized electron source as an R&D project has met the EIC R&D goals and EIC requirements by Dec. 2023 [1, 2]. The achieved parameters are shown in Table1

Parameter	**EIC R&D Goal**	**Achieved in Stable Operation**
Bunch charge [nC]	7	7.5 (12)
Peak current [A]	3.8	4.8 (No SCL)
Frequency [Hz]	1 (4 bunches)	1 (9000 bunches)
Voltage [kV]	300	320
Average Current	28 nA	30 µA
Polarization [%]	$> 85\%$	88%

Table 1: Comparison of EIC R&D goals with achieved values in stable operation

Here is a summary of the R&D achievements:

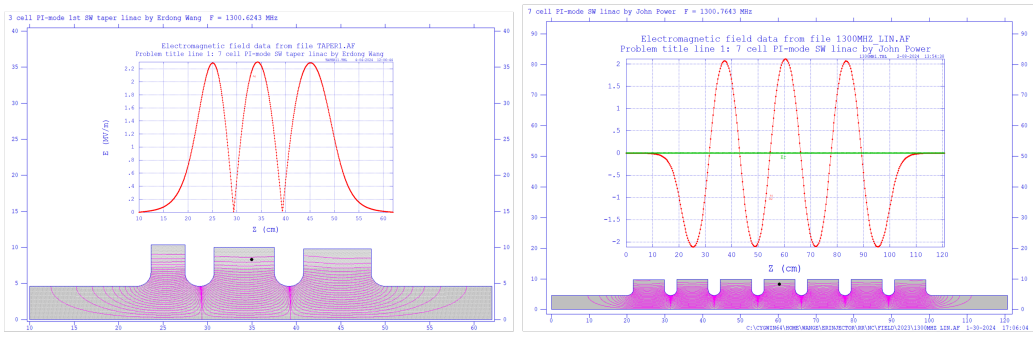
- Distributed Bragg reflector superlattice (DBR-SL-GaAs) cathodes were grown by metal-organic chemical vapor deposition (MOCVD) method between ODU/BNL/JLab collaborations. The cathode Electron Spin Polarization (ESP) was measured up to 91% at its peak QE range.
- We managed to suppress the surface charge limit by optimizing the surface doping level and cathode surface cleaning procedure.
- To address varying peak QE wavelengths due to different factors, a wavelength-tunable laser was developed.
- DBR-SL-GaAs photocathodes were successfully tested in an HVDC gun. We achieved a maximum of 11.6 nC bunch charge, 30 μA of average current, and a lifetime exceeding 2 weeks.
- We observed and explained the laser wavelength's impact on the cathode lifetime. Then, we proposed an optimal operational wavelength range for the DBR-SL-GaAs photocathode.

2.2 LINAC

The 2024 Linac studies are focused on two new schemes. i) 200 MeV NCRF 1.3 GHz linac for injection into the booster (Feb. 2024 to Jun. 2024), and ii) 3 GeV SRF linac for injection into the RCS (Jul.2024 to Oct. 2024). Additionally, progress on the high-charge Wien filter design is reported here.

2.2.1 1.3 GHz NCRF 200 MeV linac

We are considering a booster to accelerate the beam from 200 MeV to 3 GeV [3] from Feb. 2024 to Jul. 2024. This will address several of the RCS's challenges. Using the 1.3 GHz linac, we can accelerate a bunch with a much higher charge and substantially simplify the preinjector design. In this design, we are utilizing the AWA linac as shown in Fig.1b. The highly polarized electron bunch, up to 15 nC, is generated from the gun, enters two Wien filters to rotate the spin direction, and then undergoes a series of cavities involving a 98 MHz, 591 MHz buncher and a 1.3 GHz buncher to compress the bunch length from 2300 ps to 16 ps. The 1.3 GHz taper buncher utilizes 3 cells (Fig.1b) because we aim to place solenoids closer to the high peak current area without overlapping with the accelerating field. Since the beam spin direction is vertical, all the solenoids in the buncher section use reversed current to achieve $\int_{-\infty}^{\infty} B_z dz = 0$. A spin diagnostics (Mott polarimeter) will be incorporated between the buncher and linac section. Subsequently, the beam will pass through 20 sections of the 1.3 GHz linac, with each section accelerating the beam by about 10 MeV.



(a) 1.3 GHz taper cavity **(b)** Linac geometry

Fig. 1: 1.3 GHz 3 cell taper cavity and 7 cell NCRF cavity

At the end of the linac, the energy is approximately 200 MeV with an emittance of about 70/90 mm-mrad. The energy spread is around 1.2%. The beam from the preinjector is directed into a booster, where the fraction of energy spread can be reduced. Since a large energy spread is acceptable at the linac's end, the energy suppression section can be eliminated. Further optimization is still possible. The wake of the AWA cavity is notably smaller than that of the SLC linac. By utilizing ABCI, we obtained the longitudinal wake of the linac and estimated it for a 15 nC bunch with 21 cavities. The wake results in energy loss is 835 keV, and RMS energy spread is 351 keV.

2.2.2 1.3 GHz SRF linac

Another option is to use a 1.3 GHz SRF cavity, like the ILC or LCLS-II cryomodule, as the primary linac. Get the energy up to 3 GeV to avoid building a booster ring as discussed in the last section. This effort started in June 2024 and towards November 2024.

The gun to the three-cell taper section is identical to the 1.3 GHz NCRF preinjector design. After the taper cavity, we introducing a compressor at 60 MeV can further reduce the bunch length to less than 1 mm. We propose accelerating the beam to 55 MeV using two TESLA cavities with a gradient of 31 MV/m. The beam is set on an RF phase of 25 degrees to generate an energy chirp, after which it passes through a four-dipole chicane. This setup yields an rms bunch length of approximately 0.87 mm. We used 14 LCLS-II cryomodules, each containing eight 9-cell SRF cavities. Each cavity has a quadrupole and BPM. We developed a FODO lattice through the Linac section. Start-to-end tracking, including space charge and wakefields, indicates an rms energy spread of about 0.16% with rms normalized emittance about 29(x), 49(y) mm-mrad, meeting the RCS injection requirements. The chicane's R56 is -11 cm, and T566 is 17 cm. The R56 will be tunable by changing the bending angle as one knob of the bunch length.

The 3rd option was to use the 750 MeV linac and inject the beam into the 1.4 km RCS located outside of the RHIC tunnel. It reduces the number of cryomodules from 14 to 4 and keeps the rest of the design identical. This option is still under discussion.

2.2.3 High charge Wien filter considerations

Utilizing a Wien filter presents advantages over the dipole-solenoid spin rotator, including a broad energy tunable range and the avoidance of CSR issues. Initially considered for the preinjector spin rotator during the EIC pre-CDR stage, the Wien filter was discarded due to the solenoidal field overlap with the 2.856 GHz linac. It is better suited for use with a 1.3 GHz linac. Previously, the Wien filter operated only with beams below 200 keV and within 10s pC charge. For the EIC beam of 320 keV and up to 15 nC bunch charge, a longer length is required due to limitations in high voltage feedthrough. However, this conflicts with the need for a close placement of the focusing element to address high space charge. We are designing two Wien filters, each rotating the spin by 45°. Given the large beam size, a significant gap between the two electrical plates is necessary to maintain a uniform field and matched E-B fringe fields to minimize beam deflection. The design parameters for the high charge high energy Wien filter are shown in Table 2 and the preliminary design is shown in Fig.2.

To shape the electric field in the fringe region, a Rogowski profile is employed at the end of the electrode plate. The electric and magnetic fields have different decay characteristics, so nickel plates suppress the B-field in the fringe region, ensuring proper matching with the E-field in that region. Opera 3D electrostatic and magnetostatic solvers are used separately to simulate the electric and magnetic fields of the Wien filter, and results are exported in grid format for use in Parmela and General Particle Tracer (GPT). Fig. 3 shows well-matched Ey and Bx components along the center line. The electrode plate width and the transverse shaping of the iron core are optimized to achieve

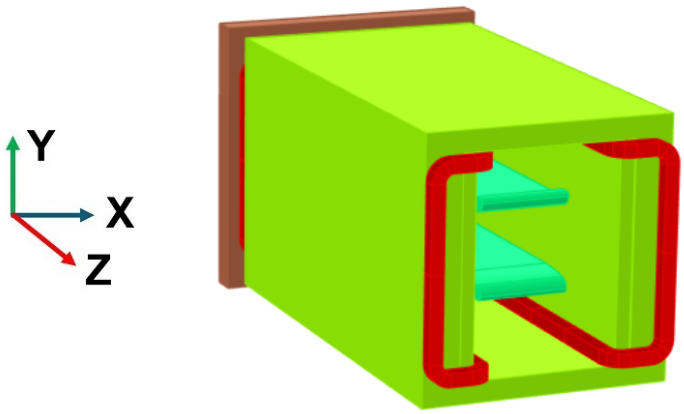


Fig. 2: Perspective view of the Opera 3D model of the Wien filter. Nickel plates are used on both sides to shape the fringe B-field. The front-side Nickel plate is not shown here to make the electrodes visible.

Table 2: Wien filter parameters

Parameter	Value
Charge [nC]	7
Energy [keV]	320
Length [m]	0.46
Ey [MV/m]	1.43
Bx [G]	60.7
Rotating angle[degree]	45
Electrode gap [cm]	7
Feedthrough voltage [kV]	50.2

field matching along the center line and in the transverse direction.

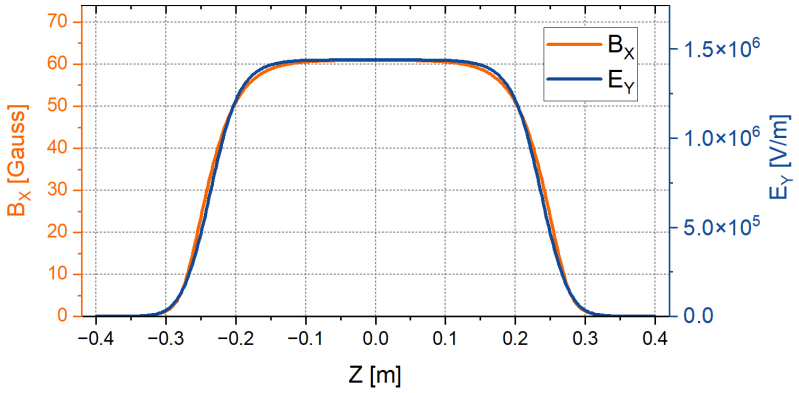


Fig. 3: Simulated electric and magnetic field generated from Opera 3D at the center-line.

Beam dynamics simulations with two Wien filters were carried out in Parmela and further checked with GPT. In Parmela, a 7.5 nC space charge-dominated beam was generated from the 320 kV HVDC gun, with the electric field map imported from Poisson simulation software. The field profiles of the solenoid, thin quadrupole lenses, and Wien filters were used to transport the 7.5 nC space charge-dominated beam. Numerous optimization steps for the electrodes and magnets

of the Wien filters were performed to minimize beam deflection in the Wien filter region. Fig. 4 shows the beam envelope of a 7.5 nC beam through Wien filter 1 and Wien filter 2. Quadrupole lenses in a triplet configuration were used before and between the Wien filters.

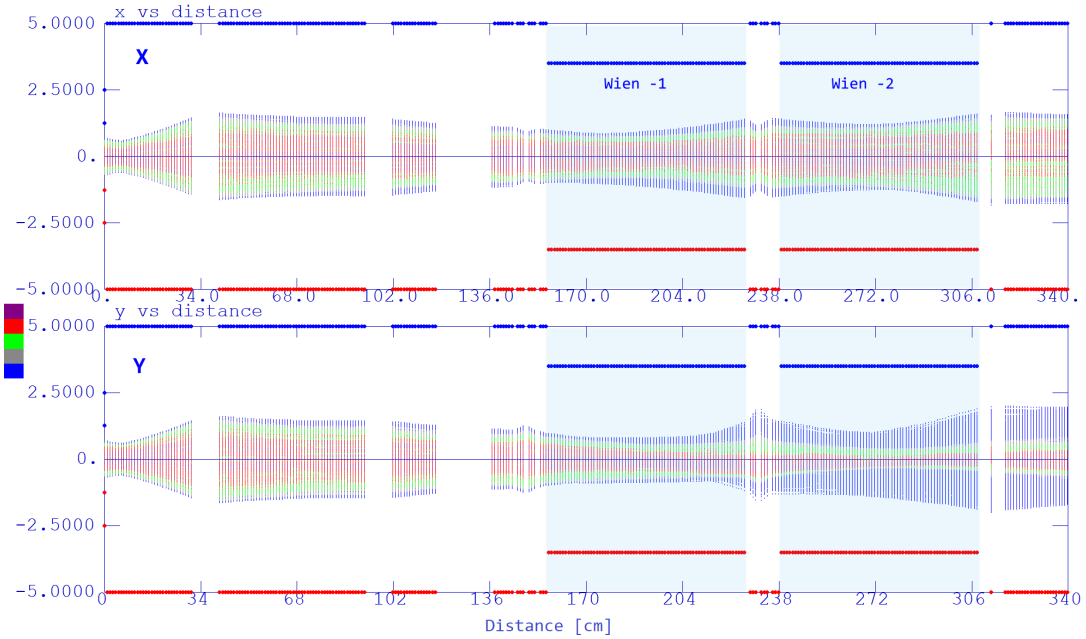


Fig. 4: Simulated beam envelope of a 7.5 nC space charge-dominated beam through Wien filters 1 and 2, obtained using Parmela.

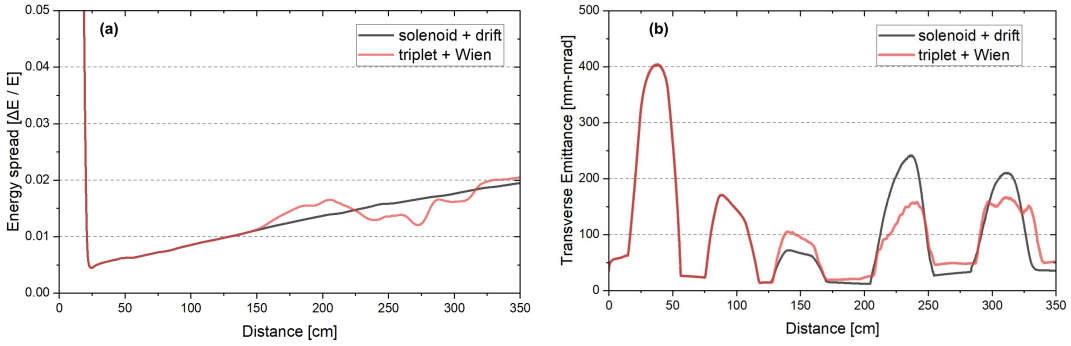


Fig. 5: The evolution of (a) energy spread, and (b) normalized transverse emittance, with respect to distance from the cathode.

The evolution of energy spread ($\Delta E/E$) and transverse emittance with respect to distance is shown in Fig. 5. The bunch length of the beam from the cathode was 1.3 ns, with a bunch charge of 7.5 nC, and in beam simulation, the space charge effect was considered. These simulations indicate that a 7.5 nC beam can pass through both Wien filters. While there is a slight increase in emittance, it does not appear to significantly affect the overall performance. Although the EIC requirement specifies a 7 nC beam, a 7.5 nC beam was considered in the simulations to provide additional margin.

One of the challenging aspects of the Wien filter is constructing the electrode and magnet to

meet the precise specifications required for maintaining uniform electric and magnetic fields. Even a minor misalignment during commissioning or the bake-out process can affect the beam trajectories. Additionally, our analysis indicates that the combined ripple from the electrode high-voltage power supply and the magnet power supply needs to remain below 100 ppm. Therefore, developing a prototype is essential to validate this unique high-charge, high-voltage Wien filter configuration.

One concern was raised up in the MAC review that space charge may impact on the spin polarization in the spin rotation. We analytically calculated the impact of space charge on spin polarization both in the Wien filter section and downstream of it [4]. The longitudinal space charge, which causes energy spread in the bunch, contributes to an ESP degradation of about 4×10^{-4} in the Wien filter range. The transverse space charge causes the following ESP degradations: 4×10^{-4} for the Gun to Wien section, 4×10^{-6} during through the Wien filter, 1×10^{-3} for ballistic compression, and 3×10^{-6} for chicane compression. The overall ESP degradation is between 1×10^{-3} and 2×10^{-3}. These analyses show that the space charge force's impact on spin polarization degradation is negligible.

GPT simulation, including 3D space charge and spin tracking, shows the spin degradation through the Wien filter is 0.0016%. Confirmed this effect is negligible.

2.3 RCS

In the past year, several changes to the lattice were required due to interferences in the RHIC tunnel and detector and the need to reduce collective effects. As a result, all the quadrupoles within 6 m on either side of IP6 and IP8 were moved, and in the non-colliding IPs, we had to move a quadrupole due to interference with the other beamlines.

As a result, we devised a new quadrupole spacing scheme for both the colliding and the non-colliding IPs. This reduced the total number of magnet families. Then, we iterated over the quadrupole strength settings until we obtained a solution that gave us good polarization transmission and dynamic aperture with an average beta function lowered from 27 to 19 m and transition gamma reduced from 57 to 40. A plot of the twiss functions are shown in Figure 6.

With these optics, we have recovered high-polarization transmission and can tolerate up to 1000 mm-mrad rms normalized emittance, achieving up to 96% transmission. This corresponds to a vertical geometric emittance at injection 170 nm (6.1 nm actual) and extraction 28.4 nm (actual 1.44 nm). The response to 100 random seeds for different alignment errors shows that we can achieve up to 95% with an average of 0.553 mm rms vertical orbit distortion (see Table 4)

We can also tolerate up to 0.5% random variation in quadrupole strength and still keep polarization transmission to 18 GeV above 95% efficient for 0.3 mm rms vertical orbit. This translates into about 1-degree vertical phase advance per arc cell random variation during the entire

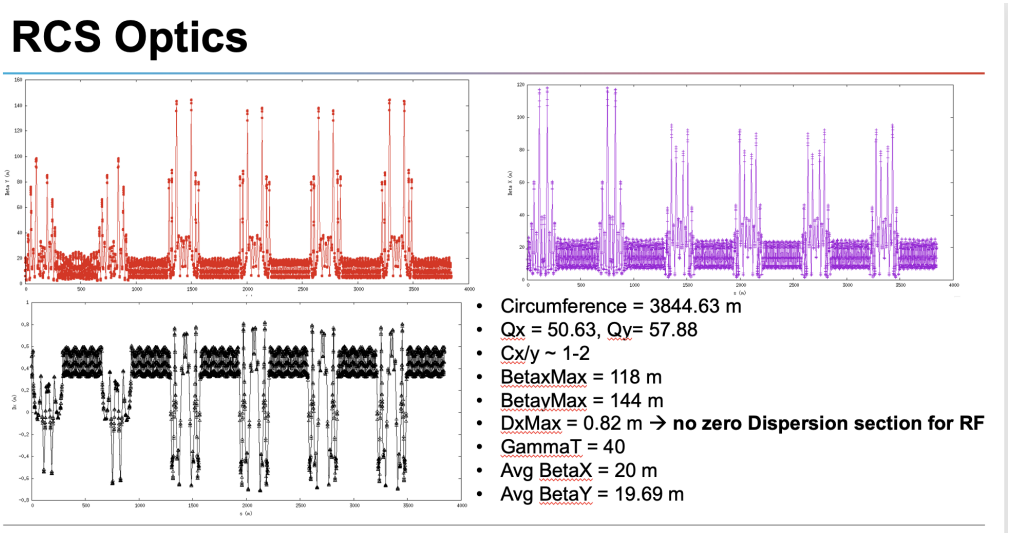


Fig. 6: The new RCS optics

Avg. Orbit RMS mm	Avg. Max Orbit mm	Pol at 10 GeV %	Pol at 18 GeV %
0.273	1.26	99	98.7
0.436	2.02	99	97
0.553	2.53	99	95.3

Table 3: Lattice Response to Imperfection Spin Resonances

ramp. This is well above the 100 ppm PS control limit and within the typical phase control of 0.1 to 0.5 degrees for electron machines.

We performed full 6D tracking of 1000 particles in BMAD with vertical, closed orbit errors of 0.59 mm RMS, including radiation. We created these closed orbit errors by randomly misaligning quadrupoles with an RMS of 2e-5 m and a 2-sigma cut-off without attempting any orbit correction. The injected emittance used was 6.1 nm in both planes with 2 mm bunch length and 0.2% dp/p rms. (see Figure 7)

We have optimized the dynamic aperture of this lattice by constraining the chromaticities to be between 0.5 and 1.5 and then minimizing the summation resonance driving terms (SRDTs) described in [5] and implemented in BMAD [6]. After optimizing using all 18 sextupole families independently, we removed sextupole families, ganged together families found to have similar absolute values of their strengths, and re-optimized. Repeating this process several times, we were able to work down to 3 independent sextupole families. The effective aperture, taking into account both the dynamic aperture and the projected physical aperture of the ring, is shown in Figure 10. We have a decent aperture out to 1.5% fractional energy offset, which is useful for stacking several bunches from the linac.

To avoid interferences, we had to introduce dipoles into the IPs, harming the periodicity that is desired for spin preservation. Before settling on the lattice described above, we experimented with

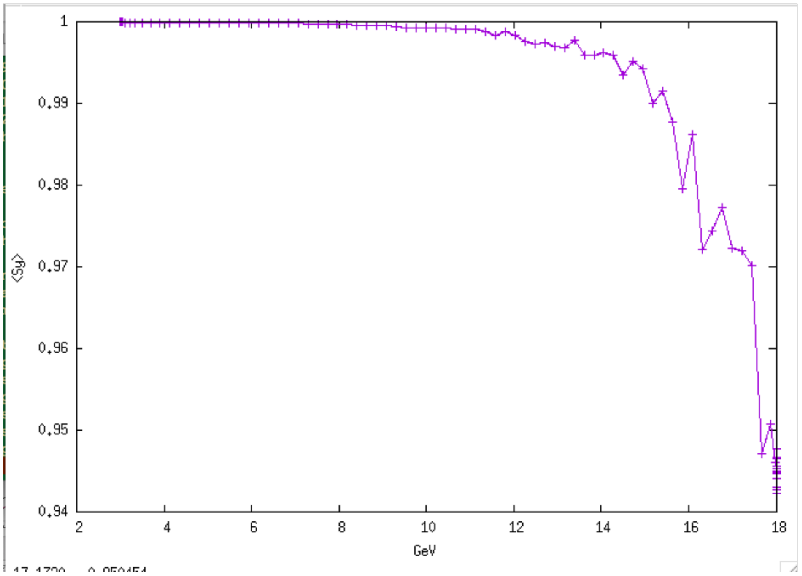


Fig. 7: 6D Spin Tracking results for 1000 particles.

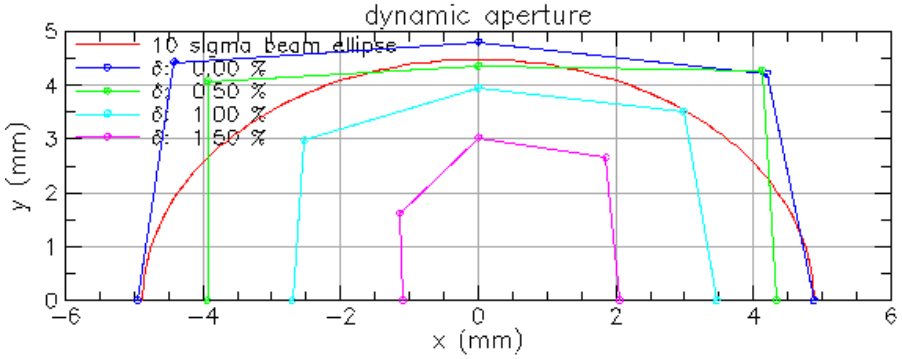


Fig. 8: Effective aperture for the RCS lattice. This combines dynamic and physical aperture, assuming a round beampipe with a 17.8 mm radius.

a scheme where we would match the transfer matrix between subsequent dipoles in the IPs to the corresponding transfer matrix between arc dipoles. To achieve this, we placed either a focusing or defocusing quadrupole after the leading dipole in the position where it would be in the arc. The rest of the drift was filled with 6 new quadrupoles, giving us the required degrees of freedom to match $\beta_{x,y}$, $\alpha_{x,y}$ and horizontal and vertical phase advance (modulo 2π) across the remainder of the drift. This was found to be quite useful in minimizing the intrinsic spin resonances, as shown in Figure 9. However, due to the extra drift length relative to what we had in the arcs, we could not match the phase advance itself but instead needed to add an additional 2π. This, in turn, required small beta functions, resulting in excessive quadrupole strengths. Since our lattice is able to achieve sufficient spin transmission without this scheme, we did not pursue this approach further.

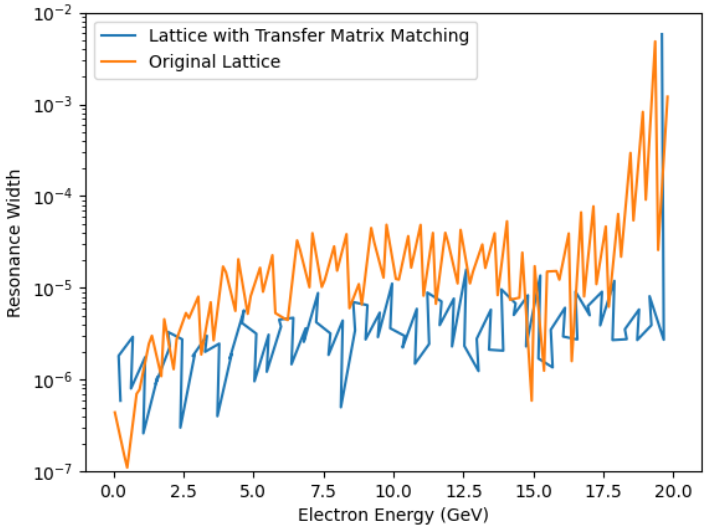


Fig. 9: Widths of the various spin resonances, both in the original optimization and when matching the transfer matrices between dipoles in the straights. This method can reduce the resonance strengths significantly. Note the vertical log scale.

2.4 Transfer lines

Based on the present design of the ESR, we have compiled a list of the following new transfer lines. The description of each transfer line listed below includes the beam injection and extraction sections associated with each transfer line. During the year 2024 some design changes have been implemented in the design concept of EIC, and these changes have affected the design of the transfer line between the various rings. In the following are described the effects on these transfer lines due to changes in the latest design changes of the EIC.

1. The hadron transfer line from the exit of the Y-AtR line to the injection point of the HSR synchrotron. This beam transfer line section has been modified, and the hadron beam from the exit of the AtR line continues with warm magnets next to the EIC ring (see description below) for the beam to be injected into the EIC ring at the IP4 location for acceleration to the final energy.

2. The electron transfer line starts from the electron gun's exit to the RCS injection point. This transfer line includes the spin rotation section of the electrons from the longitudinal direction to the vertical.

3. The electron transfer line from the extraction point of the RCS to the injection point of the ESR. This transfer line includes the beam extraction section from the RCS and the beam injection section into the ESR. This line has not been modified, and the original design of this transfer line is still valid.

The beam optics (Beta and dispersion functions) of the lines mentioned by items 1 and 2 from the list above are discussed below.

2.5 The Beam Optics of the Hadron transfer Line from the exit of the AtR Line to the Injection Point of the HSR at IP4

A preliminary description of the layout of this section is provided below. The current Y-line is designed to perform the following tasks.

1. Lower the level of the present Y-line to the level of the Hadron Storage Ring (HSR), and connect the beam transfer line to the FODO section.

2. Continue the beam line, with a periodic FODO lattice, to the beam injection section of the HSR.

3. Design an injection beam line from the exit of the periodic FODO section to the injection point of the HSR.

The design of the new HSR injection line, as described with the items 1 to 3 above, consists of normal conducting magnets and completes the beam transfer from the AGS to HSR.

This requires optical matching at each end of the transfer beamline and a beam elevation adjustment from 51.9" (YD26 Magnet Entrance) to 50" (RHIC/HSR Elevation).
In addition, the beamline must be designed in such way it does not physically interfere with other beamlines (ESR/HSR) or the tunnel.
Table 4 shows the optical beam parameters at the end of the AtR Yellow (defined as the entrance of the YD26 Magnet) and at the end of the injection septum (Hadron Injection Point).

Twiss Parameters	**AtR End**	**Hadron Injection**
$\beta_x(m)$	15.9071	65.1994
α_x	-2.4968	0.8753
$D_x(m)$	1.7577	0.0345
D'_x	0.2388	0.0015
$\beta_y(m)$	13.6397	9.2303
α_y	2.2825	-0.2563
$D_y(m)$	0.5975e-5	0
D'_y	-0.8435e-6	0

Table 4: Twiss parameters of each end of the new hadron transfer beamline. The AtR End is the entrance of the YD26 combined function magnet which exists since the RHIC program. The beamline elevation at this location is 51.9" from the RHIC/AP coordinates system. The Hadron Injection point is the exit of the HSR injection septum, which overlaps the beam center point of the HSR at IP4. The exact survey coordinates at the injection point of the EIC are (x, y, z) = (31917.47185m, 0m, 30697.74858m). The starting point of the transfer beamline is at the coordinates (x, y, z) = (31685.016119m, 0.047669m, 30275.840229m).

The conceptual design of the HSR injection beamline is complete as of January 2025. One of the main functions of this transfer line is to match the Twiss parameters at the beginning of this line with those at the end of the Y-line and the beam parameters at the end of this line with the beam parameters of EIC at the exit of the injection Septum magnet. Further optimization is underway to increase the matching quality. The beta function and dispersion plot of the beamline is shown in Fig. 10. The origin point (left end) is the end of the AtR (IP6 Direction), and the right end is the injection point (IP4 Direction). The irregular optics at each end are the matching sections that interconnects the periodic structure in the center (approximately between the 100m region and the 400m region). The periodic structure consists of combined function dipoles reused from the X-Arc of the AtR, which is not used for the EIC. This structure establishes a constant curvature needed to fit into the Sector 5 Arc of the tunnel. The beamline elevation is lowered at the first four sections of the periodic cells using three 1 meter long dipoles.

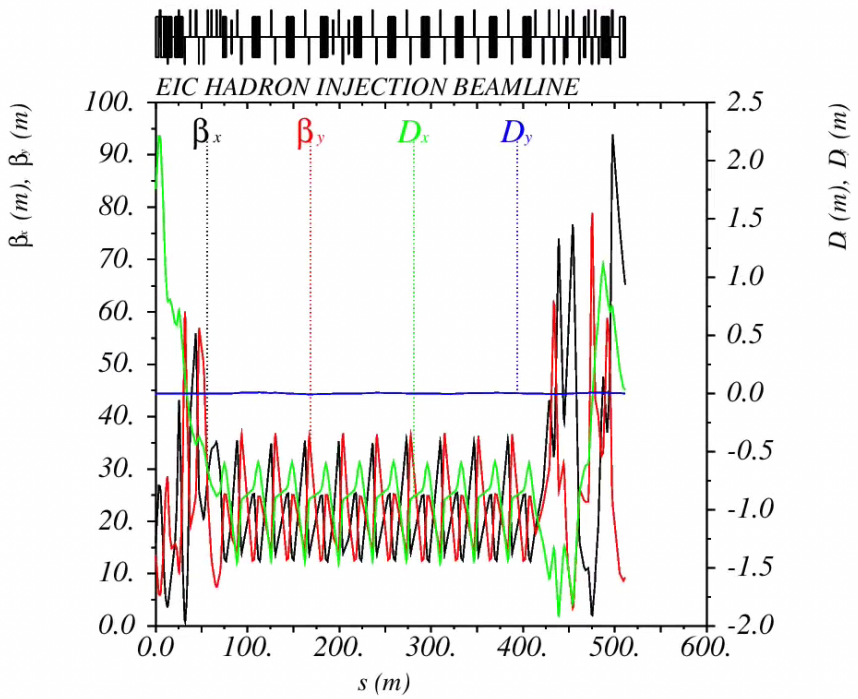


Fig. 10: Twiss parameters plot of the HSR Injection Beamline. The matching was done in such a way all other parameters (alfa and dispersion prime) and their signs would match.

The matching is being further optimized by making efforts to decrease the penalty function. In other words, the Twiss parameters are being matched towards more decimal points of the target values. After the optimization, the beamline design will undergo the system engineering by adding instruments (corrector dipoles, beam position monitors, beam profile monitors) and other auxiliary systems (power supplies, water cooling systems). The HSR transfer beamline design will then conclude with the final simulation of the hadron spin tracking, magnet misalignment, and failure scenarios. For the physics design of the periodic structure, refer to the publication

EIC-ADD-TN-079 (BNL-225059-2023-TECH).

2.6 Beam Transfer Line from the Electron Gun to the Injection point of the RCS

This original beam line has been described in detail in the paper mentioned in ref. [7]. The new design of the EIC requires a modification of this transfer line.

3 ESR

3.1 Lattice Optimization

The D1/D3 and D2 dipoles comprise the vast majority of dipoles in the ESR, including all of the arc dipoles, which are arranged in a super-bend triplet configuration. Much work has been done in maturing the lattice design to push forward the magnet designs for a Final Design Review (FDR). The D2 lengths have been set to optimize the damping decrement and emittance, and the D1/D3 length has been maximized within the physical space available [8].

Due to the tight power-supply ripple requirements arising from the beam-beam dependence on the orbit offset at the IP, the dipoles have been consolidated onto one main circuit with variable-turn coil designs and additional trim coils to switch between the configurations at different energies [9].

The interaction region (IR6) has been modified to satisfy requirements from the Compton polarimeter. Work on the spin rotators has also matured in concert with developments on the solenoid design from collaborators at CEA Saclay. The solenoid requirements have been formulated, and work is currently in progress to make space for the required vacuum components.

A design for a non-colliding IR8 with a simple cross-over that fulfills the path-length requirements to avoid collisions was developed.

The phase-advance tuning range in the non-colliding IRs was studied, and the necessary tuning ranges for the quadrupole strengths were determined. As part of this process, the positioning of the quadrupoles was also optimized. Work is in progress to investigate the option of powering the quadrupoles in small series groups with individual shunts on each quad.

3.2 Dynamic Aperture

ESR dynamic aperture (DA) has been optimized for the updated ESR lattice designs, and the effects of magnet multipole field were studied [10]. Tracking simulations were performed using LEGO code [11]. The required DA is 10σ for all ESR energies in both transverse and momentum dimensions.

Nonlinear chromaticity correction was optimized for v6.1 and v6.2 lattices. In the case of the most challenging 18 GeV lattice with two low-beta IRs, the nonlinear chromaticity correction scheme consists of 16 sextupole families distributed in six arcs and arranged in $-I$ pairs with a period of 2π for cancellation of the sextupole resonance driving terms. The scheme achieves the required $10\sigma_\delta = 1\%$ range of momentum DA at 18 GeV with the sextupole strengths within the field limit of the APS sextupole.

Dynamic aperture with errors was evaluated for v5.6 lattice using sufficiently conservative misalignment and magnet strength errors of $\Delta x = \Delta y = 0.2$ mm, roll = 0.5 mrad, and $\Delta B/B = 0.1\%$ (rms), respectively. Multipoles in quadrupoles and sextupoles were based on the APS measurement data, while dipole multipoles were estimated in the magnet design. Multipole tolerances in high-beta magnets near IP6 and IP8 were determined in earlier DA studies. For a conservative estimate, the dynamic aperture was evaluated without damping and assuming fully coupled emittance, yielding the minimum DA in 10 random error seeds of 9.5σ, 11.8σ, and 12.8σ at 18 GeV, 10 GeV, and 6 GeV, respectively, as shown in Fig. 11.

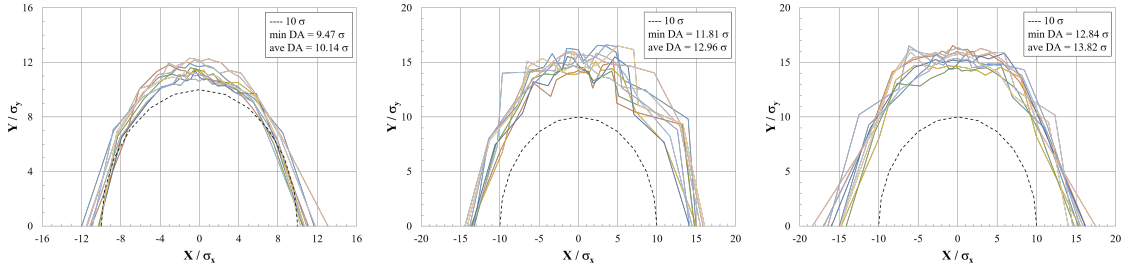


Fig. 11: ESR dynamic aperture with errors without damping: left – at 18 GeV with two low-beta IRs, middle – at 10 GeV with one IR, right – at 6 GeV with two IRs.

Dynamic aperture studies included the impact of potential degradation of field quality of the existing APS magnets, the effects of multipoles due to a large orbit and fringe field in the super-bend, and the effects of Q0EF multipoles estimated in magnet design [12]. In these studies, the measured APS multipoles in the quadrupoles and sextupoles were increased by a factor of two. The multipoles on the super-bend orbit were analytically evaluated using a sliced dipole model. Similarly, the highly nonlinear fringe field outside of the dipole body was modeled by short slices to estimate the corresponding multipoles more accurately. The studies were done for the 18 GeV lattice (v5.6) with two IRs, and the resulting impact on the DA is minimal, hence these effects are not a concern. Lastly, the impact of the Q0EF multipoles, which were estimated in magnet field calculations at the three ESR energies, including stray field from the HSR, was evaluated. In this case, the estimated Q0EF multipoles are sufficiently small yielding a slight improvement of the dynamic aperture as compared to the DA with the Q0EF multipole tolerances.

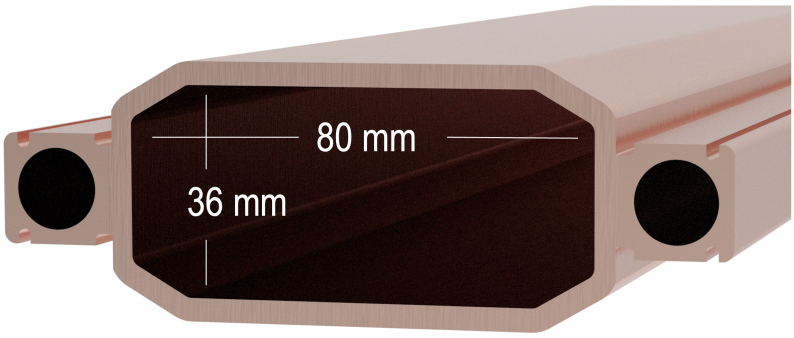


Fig. 12: The ESR vacuum chamber

3.3 Impedance and Collective Effects

The vacuum chamber profile for the ESR has been changed from an elliptical to an octagonal shape to protect the vacuum components from synchrotron radiation better. The vertical walls on the sides help keep the scattered radiation focused in the horizontal plane, making it easier to mask. Flat surfaces have been added at the top and bottom to simplify the BPM geometry installation and the pump ports' attachment. The new ESR chamber profile presented in Fig. 12 is similar to those of HERA and PEP-II.

The design of many vacuum components, such as bellows, flange joints, photon absorbers, gate valves, pumping ports, weld joints, and tapered transitions, has been changed, and the impedance budget is in the process of being recalculated.

The RF straight section is under investigation. The main focus is on simulations of the Beam Line Absorbers with parameters of $\varepsilon' = 14$, $\varepsilon'' = 3$, and $\sigma_{con} = 1.1\ S/m$ at 6 GHz provided by the RF group; two 591 MHz back-to-back cavities connected by a 90 mm beam pipe radius; gate valves; tapered transitions; ion pumps; and regular beam pipes between the cryomodules.

The longitudinal, vertical dipole and quadrupole wakefields are simulated for a 0.5 mm bunch length using different codes to benchmark the results, GdfidL [13], ECHO 2D and 3D [14], and ABCI [15].

Along with single bunch phenomena, we have also considered coupled bunch modes. The same work that tested the stability of hadrons during store also tested the stability of electrons and is discussed in detail in the HSR section [16]. For electrons, the vertical resistive wall impedance is more dangerous than crab cavities. The electrons are stable for nominal tunes and intensities with the full beam-beam model.

3.4 ESR injection consideration

The EIC is designed to achieve a high peak luminosity of $10^{33} - 10^{34}$ cm^{-2}s^{-1} through collisions of polarized electron and proton beams. The ESR is expected to deliver high-charge electron bunches

of up to 28 nC. The ESR lattice is engineered to provide a dynamic aperture of 10σ in all three planes. Due to the limited polarization lifetime, frequent electron bunch replacement is required. The swap-out injection scheme has been adopted as a baseline design to meet these demands while accommodating the constraints of the small dynamic aperture.

The RCS plays a critical role in electron accumulation, acceleration, and injection into the ESR. Beyond swap-out injection, alternative schemes, such as the injection of multiple RCS bunches into a single ESR bucket at different times and the top-up injection approach, are also under consideration. Although these methods are not part of the baseline design, they are explored to assess their potential to address operational challenges. This investigation ensures a comprehensive evaluation of different strategies to meet the stringent performance requirements of the EIC.

3.4.1 Estimate of proton emittance growth due to electron emittance mismatch in swap-out injection

The proton emittance growth is negligible in a perfect swap-out injection. However, the injection errors are unavoidable in a realistic machine. The orbit or angle error is considered in [17]. Here, we focus on the emittance mismatch.

In the RCS, the vertical emittance is nearly zero to suppress vertical intrinsic spin resonances. In contrast, the ESR maintains a finite vertical emittance to match the proton beam size at the IP. Although the electron beam can be manipulated during transport from the RCS to the ESR, maintaining precise control over the resulting emittance is challenging. This emittance mismatch during electron injection can lead to proton emittance growth.

To model the distribution evolution of both the electron and proton beams, a self-consistent simulation is required. Accordingly, we employ the strong-strong simulation method to study proton emittance growth during the swap-out injection for electron bunch charges of 7 nC, 14 nC, and 28 nC, respectively. The beam parameters used in the simulation are from [18].

The horizontal emittance of the electron beam is scanned from 5 nm to 23 nm in steps of 2 nm. The vertical emittance is scanned from 0.5 nm to 5.0 nm, with a step size of 0.5 nm. The injected electron bunches are assumed to match the ESR optics, and their initial beam sizes are determined based on the scanned emittance and beam optics. The longitudinal bunch length and momentum spread have minimal impact on the simulation. Therefore, they are set to 0.09 mm and 2×10^{-3}, respectively, which differ significantly from the design values of the ESR and RCS. The initial proton beam follows a perfect Gaussian distribution and begins interacting with the electron beam from the 1st turn. After $50,000$ turns, the electron bunch is swapped out and replaced with a fresh one, allowing the HSR bunch to continue interaction with the newly injected electron bunch.

The strong-strong simulation is influenced by numerical noise, which varies based on the model

Table 5: Model parameters during the strong-strong simulation

Model parameter	Proton beam	Electron beam
Number of macro particles	$512,000$	$1,280,000$
Number of longitudinal slices	11	11
Number of transverse grids	64×64	

parameters. The chosen model parameters are listed in Table 5. The ratio of macro particles is set equal to the ratio of bunch intensities, following our previous study [19]. To reduce computation time, we also reduce the number of longitudinal slices and transverse grids.

Figure 13 presents the proton horizontal and vertical emittance jumps for varying initial electron emittances and electron charges. Different colors represent the percentage increase in emittance per injection. The emittance increase is calculated as follows:

- The tracking data between 40,000 and 41,000 turns are averaged to obtain ϵ_1
- The tracking data between 90,000 and 91,000 turns are averaged to obtain ϵ_2
- The relative emittance growth per injection is normalized using

$$\frac{\Delta\epsilon}{\epsilon_0} = \frac{\epsilon_2 - \epsilon_1}{\epsilon_0}$$

  where ϵ_0 is the proton design value from [18].

From Figure 13, it is evident that the emittance jump is negligible for electron charges of 7 nC or 14 nC. However, for 28 nC, with smaller injected emittances (e.g. $\epsilon_x = 5$ nm, $\epsilon_y = 0.5$ nm), the vertical emittance jump reaches as high as 9.2% per injection, which is unacceptably large. Increasing the injected horizontal or vertical electron emittance helps reduce the emittance jump. When the injected electron emittance is matched to the design values ($\epsilon_x \sim 20$ nm, $\epsilon_y \sim 2$ nm), the proton emittance jump is minimized.

3.4.2 Estimate of electron loss in off-momentum accumulation

Off-momentum injection appeared to be a viable option for electron accumulation in the ESR to minimize electron bunch emittance blow-up. Our previous study shows that the proton emittance growth is also tolerable [20]. Here, we use a simple model to estimate the particle loss during this injection scheme for ESR accumulation.

Figure 14 illustrates the off-momentum injection scheme. In this approach, the injected bunch has a slightly different momentum relative to the stored bunch. A septum magnet deflects the newly injected bunch, aligning it with the off-momentum orbit. Over the next few turns, the bumped orbit is gradually reduced, allowing the injected bunch to merge with the stored bunch through synchrotron radiation damping.

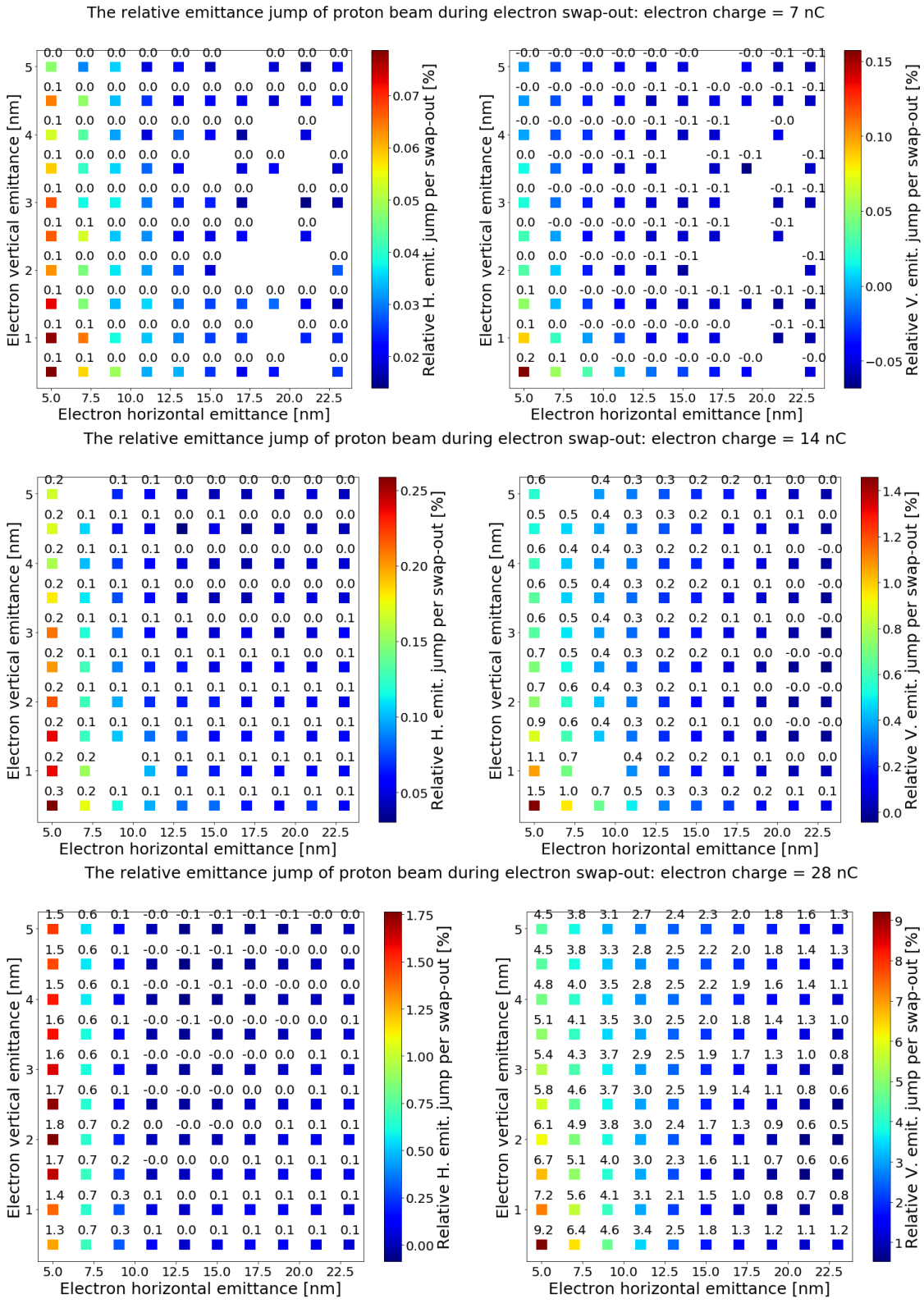


Fig. 13: Relative proton emittance growth per injection. Empty blocks indicate that the simulation was terminated accidentally, resulting in insufficient tracking data.

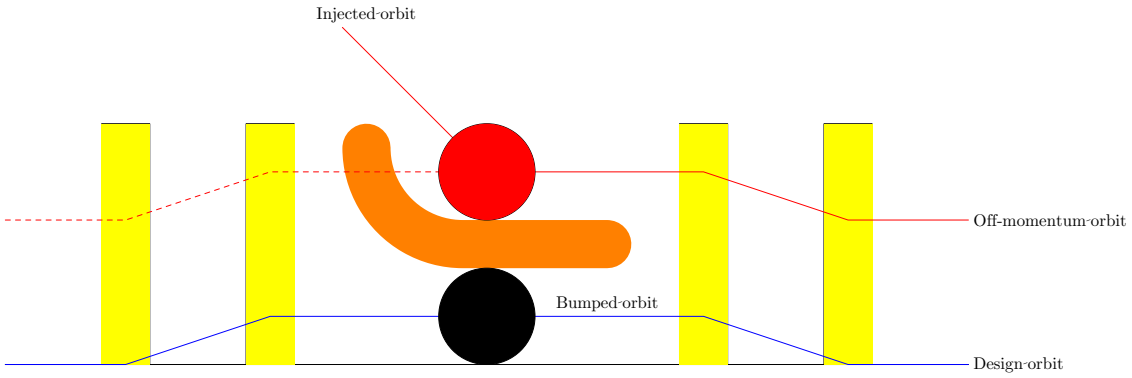


Fig. 14: The schematic for conventional off-momentum injection scheme. Kickers are shown as yellow rectangles. The orange block represents for the septum. Stored bunches are depicted as black circles, and injected bunches as red circles.

The distance between the injected orbit and the bumped orbit at the injection point is given by:

$$x_0 = w_s + n_i\sqrt{\sigma_{x,i}^2 + \eta_i^2\sigma_{\delta_i}^2} + n_s\sqrt{\sigma_{x,s}^2 + \eta_s^2\sigma_{\delta,s}^2} \tag{1}$$

where w_s is the septum thickness, while n is beam radius in terms of σ unit, η the dispersion function, and σ_δ is the RMS momentum spread. The subscript i and s refer to the injected bunch and stored bunch, respectively.

Let δ_0 denote the relative momentum offset of the injected bunch. After passing through the septum, the injected orbit overlaps with the off-momentum orbit, thus:

$$x_0 = \eta_s\delta_0 \tag{2}$$

At the moment of injection, while the position and momentum of the injected particles remain unchanged, the phase space coordinates of the injected beam will shift because the coordinate frame transitions from the injection transfer line to the ESR.

This coordinate shift is not symplectic and follows the relations:

$$\begin{aligned}
\delta_i^r &= \frac{P_0\left(1+\delta_0\right)\left(1+\delta_i\right) - P_0}{P_0} = \delta_0 + \delta_i + \delta_0\delta_i \\
x_i^r &= x_0 + x_i + \eta_i\delta_i - \eta_s\delta_i^r = x_i + \left[\eta_i - \eta_s\left(1+\delta_0\right)\right]\delta_i \\
p_i^r &= p_i\left(1+\delta_0\right)
\end{aligned} \tag{3}$$

Here, the superscript "r" indicates that these quantities are measured in the ESR frame.

Particle loss occurs either when a particle hits the septum magnet:

$$x_i^r + \eta_s\delta_i^r < w_s + n_s\sqrt{\sigma_{x,s}^2 + \eta_s^2\sigma_{\delta,s}^2} \tag{4}$$

Table 6: Parameters used to estimate particle loss and results. The parameters in gray rows were varied for optimization.

Parameter	Symbol	Unit	Arbitrary chosen	Optimized value
Injected RMS emittance	ϵ_i	nm	10.0	
Injected β function	β_i	m	20.0	11.6
Stored RMS emittance	ϵ_i	nm	25.0	
Stored β function	β_s	m	30.0	100.0
Injected RMS mometnum spread	$\sigma_{\delta,i}$	10^{-3}	2.0	
Injected dispersion	η_i	m	0.0	0.059
Stored RMS mometnum spread	$\sigma_{\delta,s}$	10^{-4}	5.5	
Stored dispersion	η_s	m	2.0	3.13
Stored bunch radius	n_s	$\sqrt{\beta_s\epsilon_s + \eta_s^2\sigma_{\delta,s}^2}$	2.5	
Injected bunch radius	n_i	$\sqrt{\beta_i\epsilon_i + \eta_i^2\sigma_{\delta,i}^2}$	2.5	2.8
Septum thickness	w_s	mm	2.0	
Particle loss	P_{loss}	%	21.9	16.1

or when the particle is outside the acceptance limits:

$$\left(\frac{x_i^r}{A_x\sigma_{x,s}}\right)^2 + \left(\frac{p_i^r}{A_p\sigma_{p,s}}\right)^2 + \left(\frac{\delta_i^r}{A_\delta\sigma_{\delta,s}}\right)^2 \geq 1 \tag{5}$$

where $A_{x,p,\delta}$ are the acceptance in the corresponding dimension in unit of σ. where A_x, A_p and A_δ represent the acceptance limits in their respective dimensions, expressed in units of σ. Typically,

$$A_x = A_p = A_\delta = 10 \tag{6}$$

The acceptance ellipse in Eq. (5) can also be defined using different norms, depending on the shape of the dynamic aperture. For convenience, we use the norm-2 definition here.

Assuming the injected beam follows a Gaussian distribution:

$$\rho\left(x_i, p_i, \delta_i\right) = \frac{1}{\sqrt{2\pi}\sigma_{x,i}} \exp\left(-\frac{x_i^2}{2\sigma_{x,i}^2}\right) \times \frac{1}{\sqrt{2\pi}\sigma_{p,i}} \exp\left(-\frac{p_i^2}{2\sigma_{p,i}^2}\right) \times \frac{1}{\sqrt{2\pi}\sigma_{\delta,i}} \exp\left(-\frac{\delta_i^2}{2\sigma_{\delta,i}^2}\right) \tag{7}$$

the survival probability can be computed by integrating over the region V:

$$P_{\text{survival}} = \int_V \rho\left(x_i, p_i, \delta_i\right) \, \mathrm{d}x_i \mathrm{d}p_i \mathrm{d}\delta_i \tag{8}$$

where the region V is defined by Eq. (4) and Eq. (5).

Obtaining an analytical solution for Eq. (8) is challenging; however, Monte Carlo sampling is well-suited for this problem. Table 6 shows the estimation result. showing a particle loss of 16.1% after optimization. This result appears not so bad.

3.4.3 Impact of Charge Decay and Top-Up Injection on Electron Bunch Polarization

Top-up injection, widely accepted in electron storage rings for maintaining beam intensity, is also considered for the EIC ESR. However, due to polarization limitations, it is not feasible for the ESR. We have explored the impact of charge decay and periodic top-up injection on electron bunch polarization in the ESR:

$$\begin{aligned} P(t) &= P_\infty + (P_0 - P_\infty)\exp\left(-\frac{t}{\tau_p}\right)\left[\frac{1-\exp\left(-T/\tau_c\right)}{1-\exp\left(-T/\tau_t\right)}\right] \qquad \text{for} \qquad 0 < t < T \\ \langle P(t)\rangle &= P_\infty + \frac{\tau_p}{T}\cdot(P_0 - P_\infty)\cdot\left[1-\exp\left(-\frac{T}{\tau_p}\right)\right]\cdot\left[\frac{1-\exp\left(-T/\tau_c\right)}{1-\exp\left(-T/\tau_t\right)}\right] \end{aligned} \tag{9}$$

where

$$\frac{1}{\tau_\mathrm{t}} = \frac{1}{\tau_p} + \frac{1}{\tau_c} \tag{10}$$

T is the duration between two injections, τ_c is the characteristic time of charge decay, P_∞ represents the asymptotic polarization, τ_p is the polarization lifetime, P_0 is the initial polarization.

Key findings include:

- **Polarization**: The polarization periodically resets to a higher value after each injection and decays until the next injection. The time-averaged polarization depends on the injection period T, charge decay lifetime τ_c, and polarization lifetime τ_p.
- **EIC Requirements**: To meet EIC's polarization goals, scenarios with specific τ_c, T, and τ_p are evaluated. For instance, achieving a 70% average polarization with a dipole field-aligned polarization state at 10 GeV requires an injection period of 5 minutes and a charge lifetime of 50 minutes.
- **Operational Constraints**: Given the intensity lifetime τ_c, the injection period T should be much smaller than τ_c. Otherwise, the injected bunch charge would not be negligible compared to the total bunch charge, which could lead to undesirable effects such as proton beam emittance growth due to beam-beam interaction.

Assuming $T/\tau_c = 0.1$, Figure 15 illustrates that the ratio τ_c/τ_p must be sufficiently small to achieve a satisfactory time-averaged polarization. For an initial spin direction opposite to the machine's preferred direction, i.e., $P_0 = -85\%$, the ratio τ_c/τ_p must be less than 0.13 to maintain an average polarization of 70%. We have assumed $T/\tau_c = 0.1$. Therefore, unless τ_p is sufficiently large, top-up injection cannot be employed to maintain the average polarization for this spin direction.

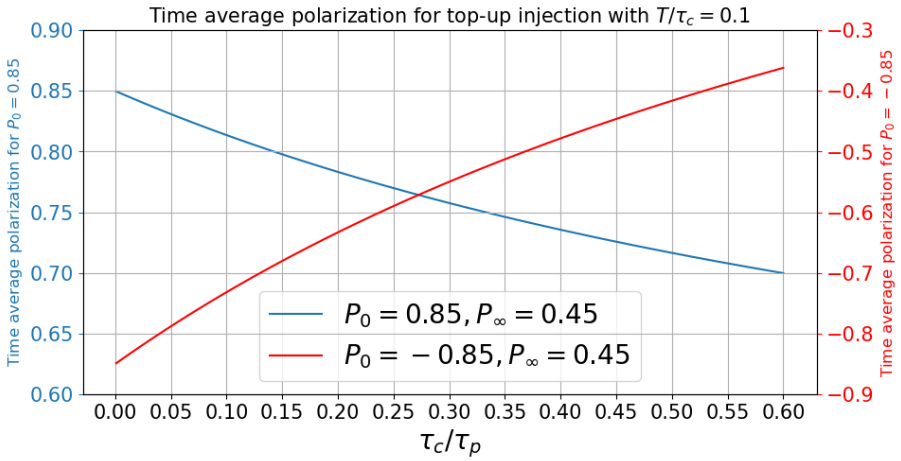


Fig. 15: Time average polarization for different τ_c/τ_p.

4 HSR

4.1 Lattice

An HSR lattice was released at the beginning of 2024 with four geometric configurations: at IR8, either having a colliding IP or a RHIC-like IR, and with the 11 o'clock arc either being the blue (outer) or yellow (inner) RHIC arc, for energies 100–275 GeV/u or 41 GeV/u, respectively. Since that release, we have replaced the longer warm dipoles used there with three (IRs 8, 10, and 12) or two (IR 4) 2 m long warm dipoles. IR4 has been reconfigured to place one of those warm dipole sets on the counter-clockwise side of the 3-o'clock triplet and the H-Jet to aid in polarimetry; the warm sections of IR4 have been laid out in significant detail. We have begun the process of changing configurations so that the high energy configurations use only RHIC yellow arcs, while the low energy configuration uses the inner blue arc at 1 o'clock.

4.1.1 HSR-IR2 update

The HSR-IR2 lattice has undergone significant updates to meet the evolving requirements of the EIC. The geometry has been redesigned to satisfy the yellow-to-yellow beam configuration, while also accommodating future integration of the 41 GeV bypass line. The current design employs existing RHIC magnet blocks.

Critical constraints have been met, including:

- Geometry: The layout has been modified to meet the yellow-to-yellow configuration and supporting future transitions to the yellow-to-blue configuration for 41 GeV operation.
- Low-Energy Beam Optics: At an injection energy of 10 GeV for gold ions, the beam optics have been successfully matched. With RHIC magnet blocks, the long drift is reduced to

160 m.

- Beam Aperture: The physical aperture requirements at injection energy are met.

The next phase of development will focus on the ramping path from low to high energies. Efforts of next iteration will also aim to restore the cooling section length to exceed 170 meters, which is essential for ensuring optimal cooling performance. Strategies include exploring the use of warm dipoles, removing unnecessary quadrupoles, and relaxing dispersion conditions to optimize the layout further.

4.2 Dynamic Aperture

According to RHIC operational experience, IR magnetic field errors play an important role in dynamic aperture reduction. With the latest 1-IR Hadron Storage Ring (HSR) lattice, we performed dynamic aperture studies for the highest luminosity collision mode involving 10 GeV electrons and 275 GeV protons. The goal of this study is to determine the tolerances of magnetic field errors from the interaction region magnets, especially for those new interaction region magnets with a large physical aperture.

For dynamic aperture calculation for the HSR, we assign artificial nonlinear magnetic field errors to all IR dipoles and quadrupoles within 100 m of the IP to evaluate their impacts on the dynamic aperture. Magnetic field errors are defined as

$$(B_y L) + i(B_x L) = B(R_{ref})L \left[10^{-4} \sum_{n=0}^{N_{max}} (b_n + i a_n) \frac{(x+iy)^n}{R_{ref}^n} \right]. \tag{11}$$

Here L is the magnet length, R_{ref} is the reference radius where the magnetic field is measured, $B(R_{ref})$ is the main field at R_{ref}, b_n and a_n are the coefficients for normal and skew magnetic components.

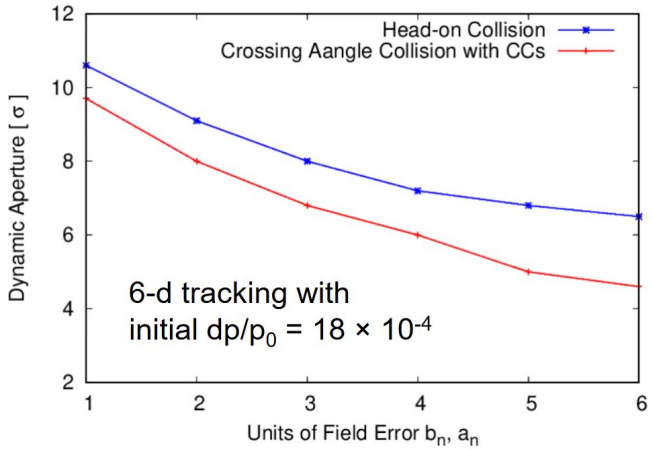


Fig. 16: Proton's dynamic aperture as a function of random IR field errors.

Figure 16 shows the dynamic aperture as a function of the relative momentum deviation dp/p_0. Here, we assume the initial $(dp/p_0)_{ini} = 18 \times 10^{-4}$, which is about three times the RMS relative momentum deviation. For this calculation, we randomly assign field errors from sextupoles to 22-poles to all IR magnets. The average dynamic aperture from 40 seeds of field errors is shown in Figure 16. The RMS value of dynamic aperture among the 40 seeds is about 1 σ. From the plot, to ensure the proton's dynamic aperture at 275 GeV is larger than 7 σ, the field errors b_n and a_n should be less than 2.5 units. According to the 255 GeV RHIC polarized proton operation, the proton dynamics aperture is about 7.5 σ. More detailed dynamic aperture calculations for field error tolerances of individual interaction region magnets are in progress.

4.3 Impedance and Collective Effects

Work on the HSR's impedance budget continues. The pseudo-Green function is calculated for a 4 mm bunch length to determine the single-bunch instability thresholds. The initial assessment of single-bunch longitudinal instability was conducted at an injection energy of 23.8 GeV, where the horizontal and vertical beam sizes are significantly reduced during the electron beam cooling process. Prior to performing particle tracking simulations with the ELEGANT code, we conducted an in-depth analysis of the Haissinski equilibrium for the longitudinal space charge impedance, with an emphasis on the effects of beam dynamics and collective forces for the proton beam. This analysis involved scaling longitudinal and energy variables for normalization and exploring the Haissinski equation under space charge conditions, leading to the derivation of the maximum space charge strength Smax, beyond which equilibrium fails. The study was further extended to scenarios incorporating higher harmonic cavities (HHC), examining their influence on bunch length and stability. These findings indicate that HHCs can support higher equilibrium currents compared to single RF systems [21]. When analyzing the space charge impedance contribution for single and dual RF systems, the instability threshold differs by a factor of 2. For the total impedance (geometric + space charge), the instability threshold differs by 50%. The instability threshold is determined through particle tracking simulations using the ELEGANT code to be I_{th}=10 mA for an energy spread of $\sigma_\delta = 7.4 \times 10^{-4}$ and horizontal and vertical emittances after colling, ε_x=20 nm and ε_x=12 nm, respectively.

Instabilities due to the crab cavities were addressed in two ways. Impedance reduction due to feedback was studied [22] as well as the efficacy of damping from the beam-beam force [16]. In the feedback study, the combination of wideband and narrow-band feedback at the betatron sidebands was shown to reduce significantly the effective impedance of the crab cavities. The system was shown to be stable in the weak coupling approximation and in a coupled mode approach with damping from a weak-strong beam-beam model. The second paper studied various models of the

strong-strong beam beam force. In this paper, the crab cavity had only a reduced quality factor due to effective feedback, resulting in a larger impedance than that used in the first paper. The beam was found to be stable for nominal beam parameters, but for certain ranges of betatron tune, there was beam-beam coupling, and the damping was lost. The loss of Landau damping was expected when the horizontal tunes in the two rings were nearly equal $Q_{xe} \approx Q_{xp}$. An unexpected result was that Landau damping was lost near what appears to be a coupling octupole resonance $2Q_{xe} + 2Q_{xp} \approx$ integer. The second effect was absent in the soft-Gaussian approximation, a full Poisson solve of the beam-beam force was needed to bring it out.

4.4 Electron Clouds

Electron clouds can have a deleterious impact on the beam quality and stability. In 2024, we studied the interaction of the highest luminosity scenario 275 GeV proton beam with the electron cloud generated in the vacuum chambers of the main arc dipoles [23]. PyECLOUD-PyHEADTAIL [24,25] simulations evaluated the impact of the electron cloud on a single bunch traveling on an axis around the hadron storage ring. The electron cloud was modeled as a uniform distribution of electrons at rest with a density equivalent to the saturation regime attained by the electron cloud during the passage of the last bunches of the beam train. The interaction was studied over a range of electron densities, which can be correlated to the secondary electron yield (SEY) value of the vacuum chamber surface. The study found that the electron cloud can drive a fast (few ms), harmful vertical emittance growth even if the SEY was as low as 1.1 in every vacuum chamber of the HSR main arc dipoles. The interaction results in a fast growth, transverse head-tail instability of higher-order mode, and a tune spread of 0.01 points in both vertical and horizontal dimensions. The study confirms the electron cloud buildup threshold previously established from analysis of the heat deposited by the electron cloud: the SEY needs to be below 1.1 at the vacuum chamber surfaces of the HSR main arc dipoles [26,27].

The beam screens for the HSR main arc magnets will have a thin film of amorphous carbon, a material that shows SEY close to 1. The presence of adsorbates can increase the SEY of the installed film to values above the electron cloud buildup threshold. Our studies have identified a beam that could be potentially used for "scrubbing" the vacuum chamber surfaces below the threshold. For a SEY of up to 1.2 in the vacuum chambers of the main arc dipoles, the highest luminosity 275 GeV proton beam in store optics generates an electron cloud that drives emittance growth (thus preventing the delivery of the intended luminosity) but survives for more than 10000 turns. Estimates find that the "scrubbing" could take a few weeks, although it might take longer in practice.

The campaign to determine the electron cloud buildup thresholds for different components of

the HSR beam line extended to the spin rotators, which have a helical dipole field. Given that the magnetic field and beam position change along the longitudinal coordinate s, the electron cloud formation was evaluated for different cross sections along the spin rotator. The results for the first spin rotator configurations found that the threshold is more relaxed (1.4) than for other HSR main arc magnets.

An accelerator physics experiment (APEX) study in RHIC evaluated the operational limitations of the RHIC octupoles for future use to mitigate collective effects like the electron cloud induced head-tail instability in the HSR [28]. The study found that the octupoles can be operated to their maximum current and generate a significant tune spread necessary for Landau damping. Data collected during the study is being analyzed. Another APEX study intended to evaluate the transition crossing with the HSR beam screens but was postponed until FY25 due to limited RHIC availability for beam studies. The design of special beam screens for the transition jump quadrupoles has started to mitigate risks associated with transition crossing.

4.5 Effect of Beam Screen Permeable Materials on Multipoles

The presence of magnetically permeable materials in the HSR vacuum chamber can introduce undesired magnetic field multipolar components that can increase chromaticity and limit dynamic aperture. In 2024, we evaluated the magnitude of the multipoles in function of the magnetic susceptibility of the main beam screen components (screen wall and cooling tube) [29]. Cold working and welding can increase the magnetic permeability of some stainless steel. While the formed parts can be annealed to remove any magnetization from cold hardening, heat treatment cannot be performed on welded parts to restore the permeability of the welds. The study found that the screen wall had to be made of extremely low magnetic permeability steel (P506 or similar) due to the wide, continuous weld that runs across one side of the screen wall, whereas the cooling pipe could be made of low magnetic permeability steel (SS316 or similar) because the weld that joins the cooling tube to the screen wall is thin and discontinuous [30].

5 Beam-beam Effects

The beam-beam simulation study activities for the EIC include beam-beam design parameter optimization for other collision modes, injection emittance mismatching from RCS to ESR, impact of delayed crab cavities in the ESR, and finalizing the tolerances for crab cavity phase noises and the ESR power supply current ripples. A good understanding has been made for the vertical emittance growth with noises and beam-beam interaction for the EIC-like flat beam collision. Additionally, we noticed that intra-beam scattering (IBS) can also drive proton vertical emittance growth with

beam-beam interaction. Some mitigation strategies have been explored, including tune optimization and using sextupoles for synchro-betatron resonance compensation. We also advanced in a GPU weak-strong beam-beam code development, which will be able to track particles element by element through the whole ring.

5.1 Design Parameter Optimization for other Collision Modes

There are several collision modes for the EIC. With a strong-strong beam-beam simulation model, we simulated and optimized the beam-beam related design parameters for the following three collision modes: 1) collision mode with 100 GeV protons with 5 GeV electrons, 2) collision mode with 100 GeV protons with 10 GeV electrons, and 3) collision mode with 41 GeV protons with 5 GeV electrons.

For the collision modes with lower proton and electron energies, it is challenging to keep the same maximum beam-beam parameters for the proton beam as the highest luminosity collision mode between 275 GeV protons and 10 GeV electrons. A large proton beam size at lower energies will sample more nonlinear magnetic field errors and reduce the proton dynamic aperture. As a possible solution, we could reduce the electron bunch intensity to reduce the proton's beam-beam parameter and increase the flatness of beams at the IP. For example, for the collision mode between 100 GeV proton and 5 GeV electrons, we have to lower the electron design bunch intensity by 30% to reduce the proton beam-beam parameters. As a result, the luminosity is also reduced by 30%.

In those studies, we ignored the effects of the space charge effect, which will play an important role in the low-energy collision modes. The space charge effect alone or combined with beam-beam interaction will reduce the maximum proton's beam-beam parameter and luminosity. Including the space charge effect in the beam-beam simulation is in progress.

5.2 Injection Emittance Mismatching from RCS to ESR

We studied the emittance mismatching tolerances for electron injection from the RCS to the ESR. Beam parameters for three electron energies, 5 Gev, 10 GeV, and 18 GeV, had been studied based on the strong-strong beam-beam simulation model. As an example, Figure 17 shows the electron beam size evolution with vertical electron injection emittance mismatching. For this simulation, the collision mode between 275 GeV protons and 10 GeV electrons was used.

The tolerance for longitudinal emittance mismatching is more tolerable than for transverse emittance mismatching, especially for vertical emittance mismatching. We need to have the vertical emittance from the RCS be at least be 80% of its design values in the ESR. More detailed 2-D injection emittance scan results can be found in the ESR injection.

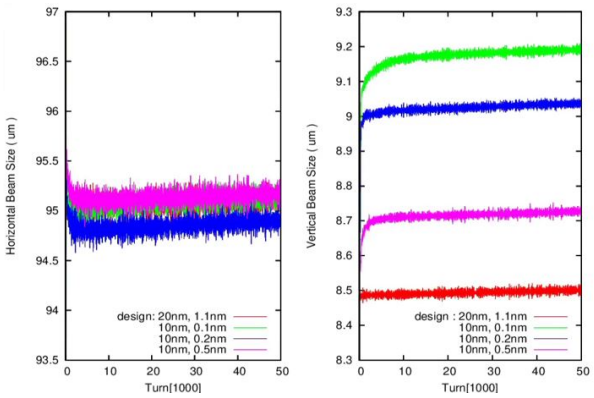


Fig. 17: Electron beam size evolution with vertical electron injection emittance mismatching.

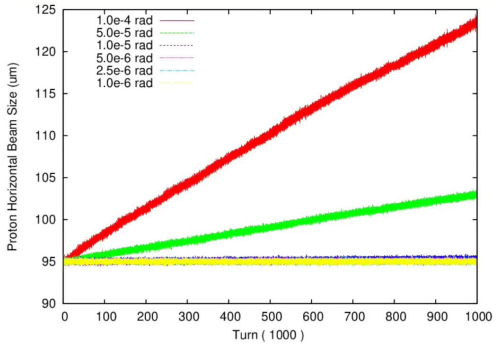


Fig. 18: Proton's vertical beam size evolution without and with horizontal cooling.

5.3 Crab Cavity Noises

It has been predicted through analytical estimation and later confirmed with beam experiments at CERN SPS that phase noises in crab cavities will generate significant horizontal emittance growth for hadron beams. We carried out numerical simulations for the HSR and confirmed the horizontal growth rates agreed well with the analytical estimates. As an example, Figure 18 shows an example of the proton's horizontal beam size evolution with different RMS crab cavity phase noises. Here, pink noise is assumed.

In addition to the horizontal emittance growth with the crab cavity phase noises, we also observed vertical emittance growth when the beam-beam interaction is included, which can be explained by the synchro-betatron resonance through flat-beam collision. To maintain a proton beam size growth rate of less than 10% per hour in both transverse planes, the RMS of pink phase noises should be no more than 1 μrad, which is beyond current state-of-the-art technology. Countermeasures under investigation include low-level RF phase feedback and active beam damper.

5.4 Crabbing Scenario Studies

We study all scenarios of crabbing schemes in the EIC. For the EIC baseline design, we will install crab cavities on both sides of the interaction region in both the HSR and ESR rings. The ideal

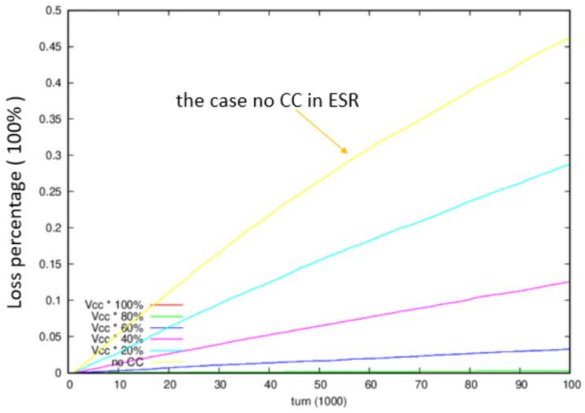


Fig. 19: Electron loss percentage as a function of proton bunch intensity if there are no crab cavities in the ESR.

horizontal phase advance between the crab cavities and the IP is 90 degrees. This crab scheme is called a local crabbing scheme since there is no crab dispersion leakage into the rest of the ring.

We examined the possibility of using a global crabbing scheme in the HSR and ESR rings. For this scheme, we only need to install one set of crab cavities on one side of the interaction region. For the HSR, due to the long proton bunch length, the global crabbing scheme will generate a large z-dependent horizontal offset in the ring, which exceeds the physical aperture. For the ESR, due to the synchro-betatron resonance between the horizontal and longitudinal motion, the electron horizontal emittance will blow up with horizontal crab dispersion leakage along the ring. Therefore, the global crabbing scheme doesn't work for either the HSR or the ESR.

There is a possibility that the 394 MHz crab cavities in the ESR will not be availbale in the beginning of EIC commissioning. We studied the impact of missing crab cavities in the ESR. Figure 19 shows the electron bunch intensity loss percentage as a function of the total crab cavity voltage of the ESR. To have stable electron motion with collision, we have to reduce the electron beam's beam-beam parameter by reducing the proton bunch intensity by half. Also, we need to keep the proton stable with the deformed electron bunch profile. In return, we may also need to reduce the electron bunch intensity. For the early commissioning of EIC, the electron bunch intensity will be one-fourth of its design value.

5.5 Beam-beam interplay with physical noise

To achieve a high peak luminosity of 10^{34} cm^{-2}s^{-1}, the hadron beam is expected to maintain a flat emittance ratio $\epsilon_y/\epsilon_x < 0.1$ for several hours. However, we have observed vertical emittance growth in simulations:

- **Strong-strong simulation**: It turns out the numeric noise dominating the emittance growth.
- **Beam optics imperfections**: The beam-beam performance can be restored with sufficient

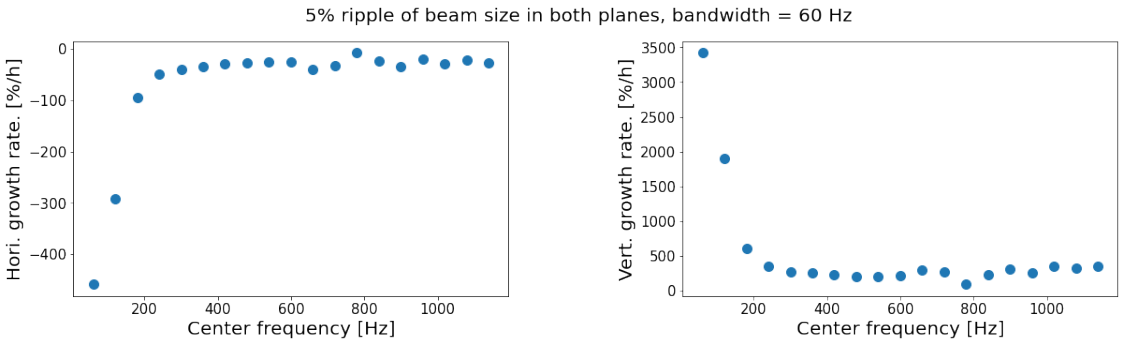


Fig. 20: Proton emittance growth with 5% electron size ripple. The ripple is a narrow band distortion. Its bandwidth is chosen as 60 Hz, and the center frequency is scanned from 60 Hz upto 1200 Hz.

knobs.

- **Physical noise**: It is unavoidable in real machine, and may be the bottleneck to future operation.

We have applied weak-strong simulations to study the interplay between beam-beam interactions and physical noise. The findings related to orbit ripple were published in [31]. The effects of electron size ripple and proton IBS diffusion are briefly discussed in the following sections. These results have been presented in [32].

5.5.1 Electron size ripple

Figure 20 illustrates proton emittance growth under a 5% electron size ripple. Emittance transfer is evident, with significant vertical emittance growth accompanied by a notable reduction in horizontal emittance. The dangerous frequency is approximately 60 Hz, corresponding to the AC frequency in the US. Further analysis indicates that a 0.1% size ripple serves as the threshold for a 10%/h emittance growth rate.

5.5.2 Proton IBS diffusion

Figure 21 shows the tracking results with and without IBS diffusion or cooling effects. The particles are tracked for 1 million turns, equivalent to approximately 12.8 seconds. It is reasonable to assume that the IBS time remains constant during tracking. Consequently, the IBS diffusion and cooling processes are modeled using the simplified equations:

$$\lambda_u = \exp\left(-\frac{T_{\text{rev}}}{\tau_u}\right), \qquad u_{n+1} = \lambda_u u_n + R_u \sigma_u \sqrt{1-\lambda_u^2} \tag{12}$$

where $u = x, p_x, y, p_y, z, p_z$ represents the phase space coordinate, T_{rev} the revolution time, τ_u the characteristics time of IBS diffusion, σ_u the RMS size of corresponding plane, and R_u the random

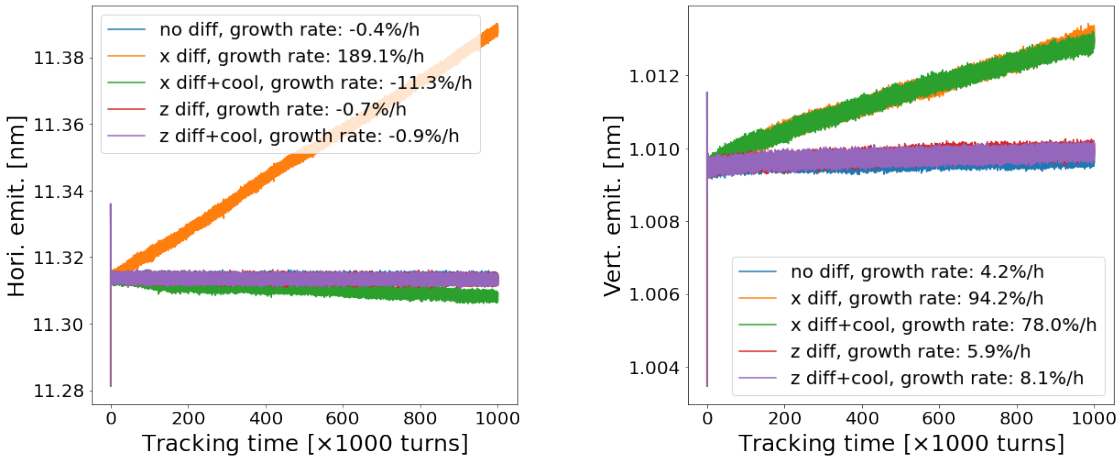


Fig. 21: Proton emittance evolution with and without IBS diffusion or cooling.

number following standard Gaussian distribution.

Figure 21 illustrates that horizontal IBS diffusion significantly contributes to vertical emittance growth. However, horizontal cooling does not mitigate this vertical emittance increase. Longitudinal IBS diffusion and cooling have minimal effect on transverse emittance growth. It is crucial to suppress the excessive vertical emittance growth.

A journal paper is in preparation to understand these simulation results, and the mitigation strategies are under consideration.

5.6 GPU-Parallelized Weak-Strong Beam-Beam Simulation Code

As the scale of the EIC project continues to expand, simulations with more realistic models are critical to the design. Therefore, developing a high-performance and extendible simulation code is indispensable. On the one hand, the code should be fast so that a simulation with complicated models can be finished in a reasonable time. On the other hand, the code needs to be extendable so that new models and functionalities can be easily added. We developed a GPU-parallelized weak-strong beam-beam tracking code using the Julia programming language. We choose the Julia language for the reasons below:

- Julia uses LLVM as a backend to compile the program to efficient native code and can be as fast as the C programming language.
- Julia adapts multiple dispatch to achieve polymorphism and can easily express many design patterns from other programming paradigms.

We benchmarked our newly developed GPU code against our previously developed C++ code. We performed beam-beam simulation for HSR using both codes with the parameters listed in CDR [18], and our result shows good agreement in the turn-by-turn emittance tracking. (Fig. 22)

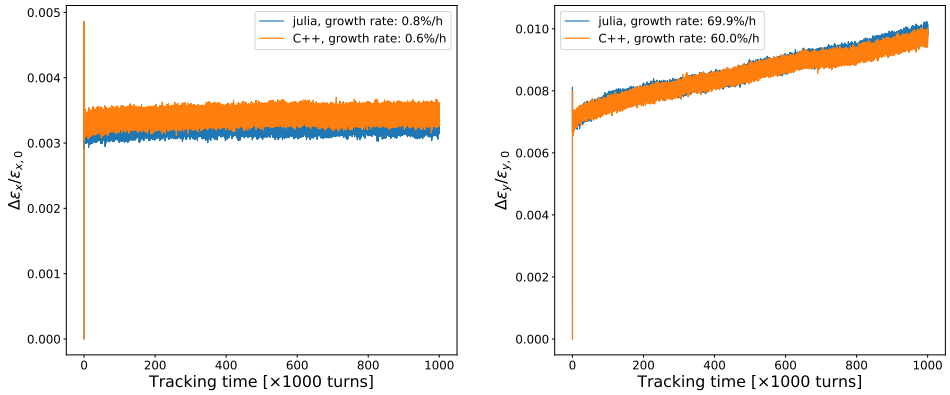


Fig. 22: Turn-by-turn emittance tracking for HSR using our two developed codes. Proton beam is crabbed with 394MHz crab cavity. Detailed parameters can be found in [18]

6 Beam Cooling

6.1 1D Simulations of Microbunched Electron Cooling (MBEC)

We have continued our simulations of MBEC as a possible implementation of strong hadron cooling (SHC). We had previously written a code to model the passage of hadrons and electrons through the cooler considering only longitudinal motion and modeling inter-particle forces with a z-dependent disc-disc interaction function, thereby deriving a simulated wake function [33]. While we maintain the 1D interaction function for ease of computation, we have updated the code to allow the electrons and hadrons to move in the full 6D phase space; from the BMAD lattice for the cooler, we extract the transfer matrix for the electrons at each time step and use this to appropriately update their positions. In addition, we add in the second-order delay due to non-zero transverse angles. We have found that, despite the short lengths of the electron chicanes relative to the lengths of the amplifier straights, their large Courant-Snyder gamma functions introduce a strong second-order transverse dependence on the electron delays, significantly smearing out the wake. See Figures 23 and 24.

6.2 Luminosity Model

We have developed a model of the evolution of the hadron bunch parameters and the corresponding changes in the luminosity over the course of the store. We track a bunch of hadron macroparticles through a HSR lattice consisting of a handful of transfer matrices, plus RF kicks depending sinusoidally on each particle's longitudinal position. We wish to simulate the bunch evolution on timescales of roughly 10 hours, corresponding to approximately 3 billion turns. In order to run the simulations in a reasonable time, we let each simulated turn model $N = 10^6$ real turns, increasing the incoherent kicks to particles in the beam by a factor of $\sqrt{N}$ and increasing the coherent kicks

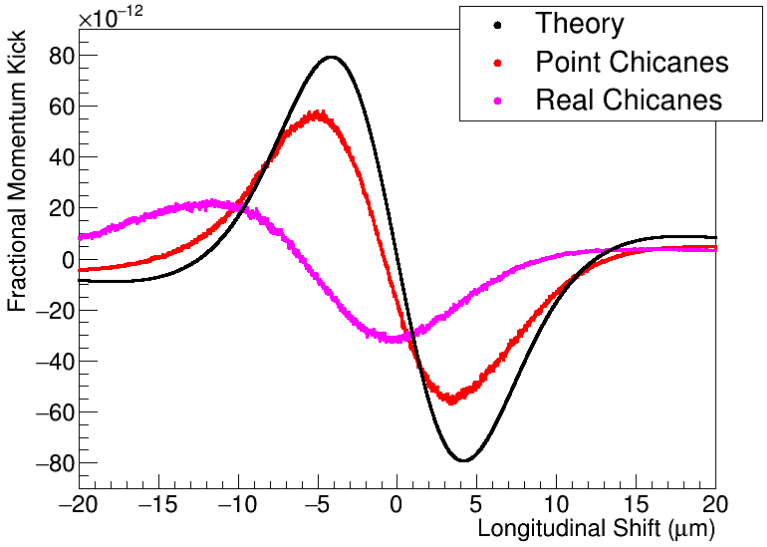


Fig. 23: 100 GeV theory wake, simulated wake assuming that chicanes are simple R_{56} elements and simulated wake with realistic chicanes. We see significant harm to the wake when using real chicanes due to the large Courant-Snyder gammas introducing second-order delays for the electrons.

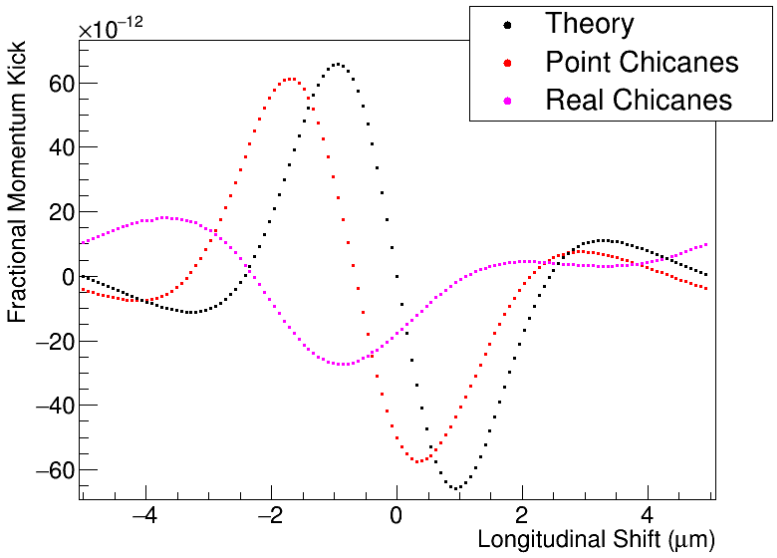


Fig. 24: 275 GeV theory wake, simulated wake assuming that chicanes are simple R_{56} elements and simulated wake with realistic chicanes. We see significant harm to the wake when using real chicanes due to the large Courant-Snyder gammas introducing second-order delays for the electrons.

by a factor of N.

The rate of intrabeam scattering (IBS) is calculated using the method of [34], which rewrites the Bjorken-Mtingwa IBS formulas [35] in terms of easily-computed elliptic integrals. The lattice optics are evaluated at 1000 equally-spaced points around the ring using the single-IR 275 GeV HSR lattice. The optics for other energies are assumed to be sufficiently similar. The horizontal and vertical emittance are taken from exponential fits to the distribution of hadron actions, and the bunch length and energy spread are taken from Gaussian fits to the distributions of the longitudinal

positions and momentum deviations. Using fits here emphasizes the core of the bunch rather than the tails that can be produced, particularly under the influence of cooling. Once the rate is known, each particle receives a Gaussian random kick to its momentum in each of the three planes. The size of the kick for a given macroparticle is scaled so that the expected increase in action for a given macroparticle is proportional to the local spatial density of nearby hadrons and so that the total heating rates match the IBS theory. For beam-beam growth, we provide each hadron macroparticle with Gaussian random kicks horizontally and vertically so that the total growth time is 20 hours horizontally and 5 hours vertically. Due to the complicated nature of this interaction, no spatial dependence is assumed.

Microbunched electron cooling can be included in this simulation. A modulator and kicker element are introduced in the lattice, and each hadron receives a coherent energy kick in the kicker based on its delay in moving between the two elements and its transverse coordinates in each. Additionally, Gaussian random energy kicks are applied to simulate heating due to diffusion. See [36] and the references therein for additional details.

A particle is declared lost if its actions violate the constraint

$$J_x/J_{x,max} + J_y/J_{y,max} + J_z/J_{z,max} < 1 \tag{13}$$

where $J_{x,max}$ and $J_{y,max}$ are the transverse actions that would send a hadron beyond 6 times the initial beam size in the relevant plane, and $J_{z,max}$ is the size of the 197 MHz RF bucket.

The electron beta functions at the interaction point (IP) are adjusted over the course of the store to keep the electron beam size matched to that of the hadrons. If the hadron beam horizontal or vertical emittance increases above its initial value, the corresponding hadron beta function at the IP is increased to maintain a constant beam divergence so as to minimize background on the forward detectors. If the hadron beam's emittance would decrease below its initial value, primarily due to cooling, the beta function is also increased so that we never need to reduce the electron betas below their initial values.

Instantaneous luminosity is calculated using the formula from [37]:

$$\mathcal{L} = 2cf_{rep} \int \rho_+(\vec{x},t)\rho_-(\vec{x},t)d^3\vec{x}dt \tag{14}$$

We evaluate this integral numerically by tracking the individual hadron macroparticles in the vicinity of the IP, integrating the local electron density each sees as a function of time (taking into account that the electron beam is moving longitudinally and that the electron betas increase as we move away from the IP), summing the results, and multiplying by the number of real particles

represented by each macroparticle. We assume that the crab cavities work perfectly so that the electrons and hadrons collide head-on and that the electron beam is perfectly Gaussian.

We show the luminosity as a function of time for 275 GeV protons colliding with 10 GeV electrons in Figure 25, both with and without microbunched cooling at the store. We set the luminosity equal to 0 for the first half hour of the store because this is when we will fill electrons and turn on the detector. We also show the average luminosity for various store lengths in Figure 26, where we assume that we have an additional 2-hour downtime between stores in order to fill the hadrons, do injection cooling, and ramp. We are able to get $2.1 \times 10^{33}\text{cm}^{-1}\text{s}^{-1}$ average luminosity without cooling at store, which roughly doubles to $4.0 \times 10^{33}\text{cm}^{-1}\text{s}^{-1}$ with strong hadron cooling.

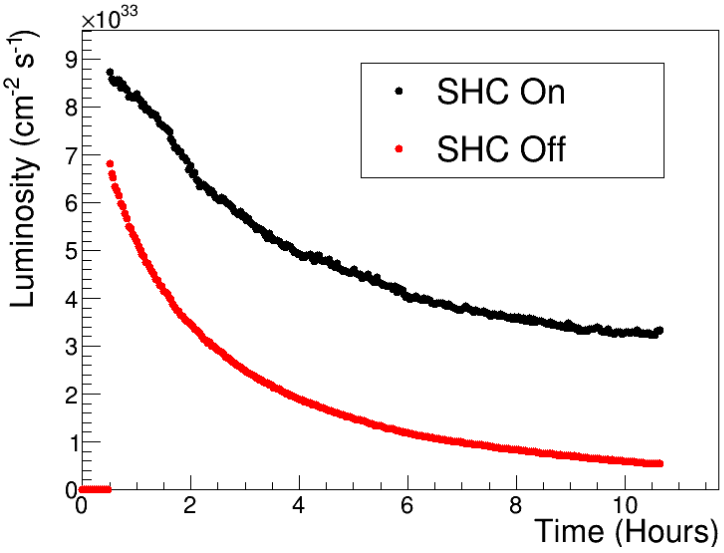


Fig. 25: Instantaneous luminosity for 275 GeV protons colliding with 10 GeV electrons, both with and without strong hadron cooling at the store. Luminosity falls in both cases but is somewhat mitigated by the cooling.

6.3 3D analysis of Microbunched Electron Cooling (MBEC)

A set of fully three-dimensional theoretical and simulation techniques has also been developed for the study of microbunched electron cooling (MBEC) [38]. Our model incorporates previously neglected features and effects, such as the point charge nature of the electrons, as well as their angular spread and transverse motion (betatron oscillations). A three-dimensional macroparticle simulation algorithm, along with a Vlasov equation-based, frequency-domain theoretical formalism, have been used to track the modulation of the electron beam along the entire cooling lattice, allowing us to perform a comprehensive study of the generalized wakefield of the system (a key figure of merit for the cooler). In general, good agreement has been observed between theory and simulation-based approaches (see Figure 27). Moreover, the results from our 3D toolkit have been compared to their counterparts from simplified but computationally faster approximate models

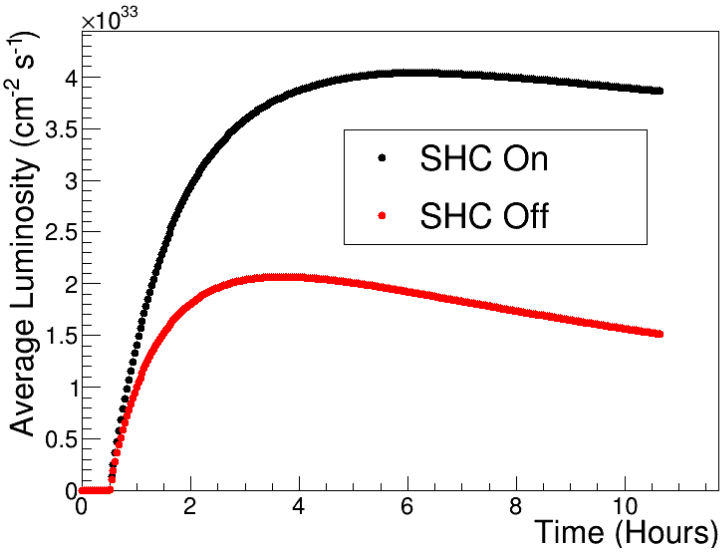


Fig. 26: Average luminosity as a function of store time for 275 GeV protons colliding with 10 GeV electrons, both with and without strong hadron cooling. We add an additional two hours in the denominator to account for filling the protons, injection cooling, and ramping. We can reach an average luminosity of $2.1 \times 10^{33}\text{cm}^{-1}\text{s}^{-1}$ without strong hadron cooling at store, and $4.0 \times 10^{33}\text{cm}^{-1}\text{s}^{-1}$ with cooling.

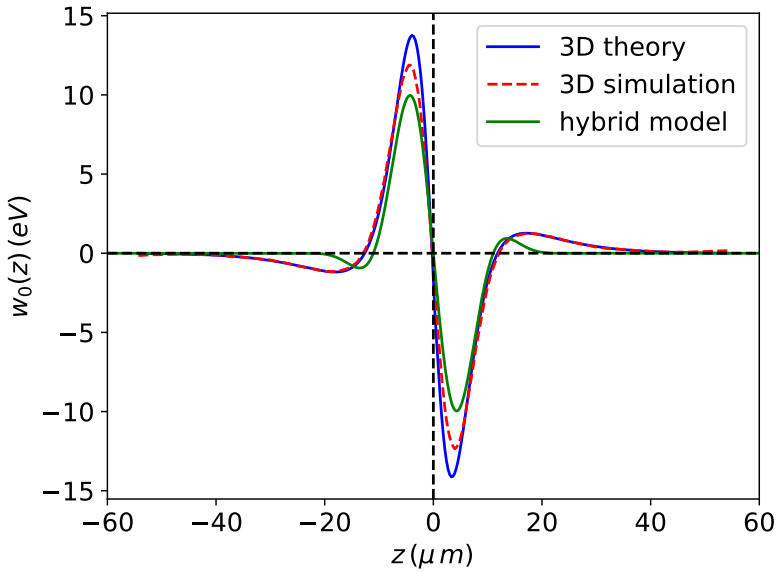


Fig. 27: On-axis wake profiles for the peak electron current. Here, w_0 (which represents the total energy change of the kicker proton) is plotted versus the longitudinal offset z. Data shown are from 3D theory (blue solid lines), 3D simulation (red dashed lines), and the hybrid model (green solid lines). The hybrid model data are courtesy of W. Bergan.

(disk-based or hybrid) used for optimization purposes. For the parameter set considered here (based on the EIC baseline for 100 GeV protons and assuming a cooler electron beam with a 10 A peak current), the 3D calculation essentially confirms the validity of the performance figures from the approximate models. In conclusion, although computationally intensive and relatively slow, the 3D model provides a necessary complement and benchmark for faster but less rigorous techniques, such as the hybrid model, as the sufficient accuracy of the latter cannot be taken for granted.

7 Beam-physics-driven specifications for the ESR magnet power supply ripple

The ESR requires stringent tolerances for beam position and size stability at the interaction point (IP) because oscillations in the electron beam at frequencies ranging from sub-Hz to the proton betatron frequency and its harmonics can result in unacceptable proton emittance growth [39,40]. In FY24, significant effort was dedicated to translating these tolerances into engineering specifications for various technical systems, with a particular focus on the ESR magnet power supplies (PS). This work necessitated a quantitative understanding of two critical aspects: how the current ripple of individual magnet power supplies affects the electron beam's position and size oscillations at the IP and the extent to which magnetic field oscillations are attenuated by eddy currents in the vacuum chamber.

The eddy current shielding effectiveness for the currently adopted vacuum chamber cross-section was evaluated both analytically and via FEM simulations [41]. Detailed studies were also conducted to address the beam dynamics, with engineering specifications for the main magnets and corrector PS being documented across various design records and a partial physics summary provided in [42,43].

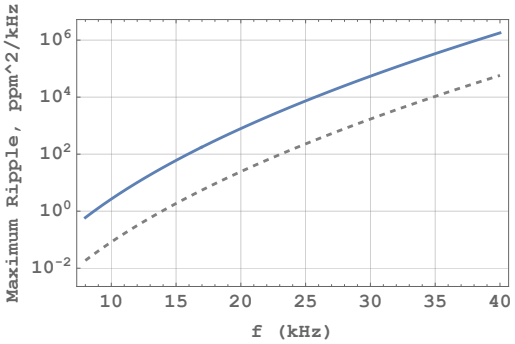


Fig. 28: (solid) Maximum allowable rms current ripple; (dashed) same for axially-symmetric chamber approximation and the (now obsolete) original powering scheme with $I_{\text{dipole}} \propto E$ for most dipoles.

As an illustrative example, we describe the high-frequency dipole PS current ripple specification, shown in Fig. 28. It was derived to ensure an RMS positional stability of $10^{-4}\sigma$ at the IP within the 8–40 kHz frequency range, as dictated by beam-beam physics requirements [39,40]. The magnetic field ripple tolerances were translated into dipole PS current ripple specifications, accounting for the attenuation provided by the vacuum chamber.

A preliminary analysis of this specification, resulting in the dashed line, was conducted previously [42,44]. However, in FY24, it was significantly updated [43] to reflect the currently adopted vacuum chamber cross-section and the new ESR dipole magnet powering scheme.

As shown in the figure, the updated specification is more than 30 times less restrictive, providing

significantly greater flexibility in selecting the dipole PS.

8 The effect of the crab cavities on the beam polarization in the HSR

At the interaction point, beams intersect at a crossing angle of 25 mrad, which would significantly reduce luminosity. To counteract this effect, two RF crab cavities are placed on the upstream and downstream sides of the IP [18]. As the particle bunches pass through the crab cavities, they are rotated by half the interaction angle to maximize luminosity, meaning that the head and tail of the particle bunches deviate from the nominal orbit. The phase advance between the crab cavity and the IP6 in the HSR is close to, but not exactly, 90°. As a result, the spins of the head and tail particles receive a horizontal kick. This can potentially lead to polarization spreading and a reduction in the longitudinal spin component.

The orbit kick induced by the crab cavity is given by: $\theta = \frac{q}{\gamma}(E+B)$, where q is the particle charge, γ is the Lorentz factor, and E and E represent the electric and magnetic fields of the crab cavity. The corresponding spin kick in the orthogonal magnetic field approximation is $\alpha = qG(E + B)$, where G is the anomalous magnetic moment of the particle. This establishes a linear relationship between the orbit kick θ and the spin kick α, expressed as: $\alpha = G\gamma\theta$.

The particle coordinates can be obtained from a Bmad particle tracking simulation, which includes the implementation of dipole correctors at the crab cavity locations. The one-turn matrix for spin rotation around the HSR, which incorporates spin rotators, snakes, and crab cavity kicks, determines the direction of the stable spin axis. This can be expressed as: $\vec{a} = \frac{1}{2}sin(\frac{\phi}{2})Tr(\vec{\sigma} \cdot T_{turn})$, where ϕ is the spin precession angle per turn, $\vec{\sigma}$ represents the Pauli matrices, and T_{turn} is the one-turn transfer matrix [45].

The most significant effect on polarization is observed for protons at 275 GeV. In this case, the tilt of the stable spin axis in the radial direction is approximately 11 mrad, see Fig. 29. This corresponds to a reduction in the average longitudinal polarization of the bunch by about 0.01%. However, this reduction is negligible and does not significantly impact the overall polarization.

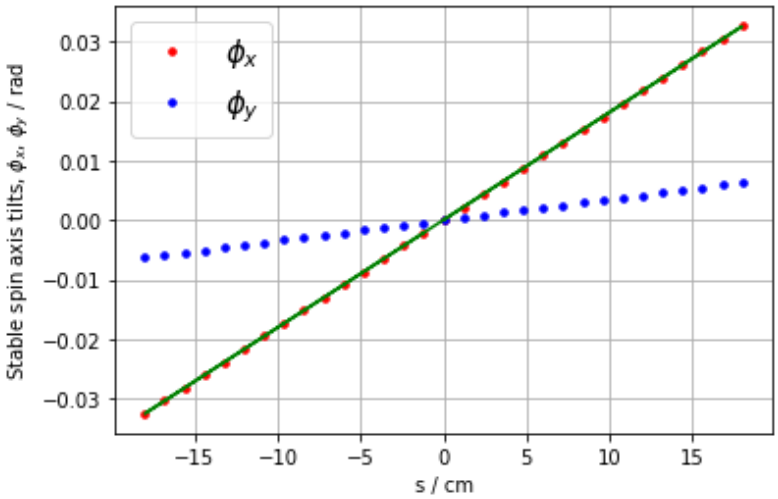


Fig. 29: The invariant spin axis tilts in both the radial (ϕ_x, red) and vertical (ϕ_y, blue) directions, depending on the distance from the center of the bunch. The tilt in the radial direction is the dominant effect.

9 Summary

The report summarizes recent advancements in the Electron-Ion Collider (EIC) project for FY 2024. Work supported by Brookhaven Science Associates, LLC under Contract No. DE-SC0012704 with the U.S. Department of Energy.

References

[1] Erdong Wang, Omer Rahman, Jyoti Biswas, John Skaritka, Patrick Inacker, Wei Liu, Ronald Napoli, Matthew Paniccia; High-intensity polarized electron gun featuring distributed Bragg reflector GaAs photocathode. Appl. Phys. Lett. 17 June 2024; 124 (25): 254101. https://doi.org/10.1063/5.0216694

[2] Erdong Wang, Omer Rahman, John Skaritka, Wei Liu, Jyoti Biswas, Christopher Degen, Patrick Inacker, Robert Lambiase, and Matthew Paniccia Phys. Rev. Accel. Beams 25, 033401 https://doi.org/10.1103/PhysRevAccelBeams.25.033401

[3] E. Wang *et al.*, "The design progress of a high charge low energy spread polarized pre injector for electron ion collider", presented at IPAC 2024, Nashville, TN, USA, May 2024, paper MOPC24. DOI:10.18429/JACoW-IPAC2024-MOPC24

[4] Wang, Erdong. "Space Charge Effects on Spin Polarization in High-Intensity Preinjector." , Nov. 2024. https://doi.org/10.2172/2478783

[5] J. Bengtsson, “The Sextupole Scheme for the Swiss Light Source (SLS): An Analytic Approach”, SLS Note 9/97 (1997).

[6] D. Sagan *et al.*, BMAD, `https://www.classe.cornell.edu/bmad/`

[7] N. Tsoupas et. al. International Journal of Modern Physics A Vol. 34, No. 36 (2019)

[8] D. Marx et al., "Design Updates to the EIC Electron Storage Ring Lattice", in Proc. IPAC'24, Nashville, TN, May 2024, pp. 234-237. doi:10.18429/JACoW-IPAC2024-MOPC73

[9] F. Zulferino et al., "ESR Dipoles (D1/D3 & D2) Magnets Performance Requirements Document". https://brookhavenlab.sharepoint.com/:b:/r/sites/eic-document-center/

[10] Y. Nosochkov *et al.,*, “Dynamic Aperture of the EIC Electron Storage Ring,” in Proc. IPAC'24, Nashville, TN, May 2024, paper MOPC82.

[11] Y. Cai, M. Donald, J. Irwin, and Y. Yan, “LEGO: a modular accelerator design code,” in Proc. PAC'97, Vancouver, B.C., Canada, May 1997, pp. 2583-2585.

[12] B. Parker, “B0 field harmonics,” presented at EIC Lattice Workshop, BNL, Upton, NY, USA, Oct. 2022, unpublished.

[13] W. Bruns, http://www.gdfidl.de

[14] I. Zagorodnov, “Indirect methods for wake potential inte- gration”, Phys. Rev. ST Accel. Beams, vol. 9, p. 102002, 2006. doi:10.1103/PhysRevSTAB.9.102002

[15] Y. H. Chin, https://abci.kek.jp/abci.htm

[16] J. Qiang, M. Blaskiewicz, "Strong-strong simulations of combined beam-beam and wakefield effects in the Electron-Ion Collider" NIMA, 1069 (2024) 169942.

[17] J. Qiang, M. Blaskiewicz, Y. Hao, Y. Luo, C. Montag, F.J. Willeke, and *et al.*, “Transient Beam-Beam Effect During Electron Bunch Replacement in the EIC”, in *Proc. IPAC'21*, Campinas, SP, Brazil, May 2021, pp. 3228–3231. `doi:10.18429/JACoW-IPAC2021-WEPAB252`

[18] F. Willeke, "Electron Ion Collider Conceptual Design Report 2021", BNL-221006-2021-FORE, 2021. `doi:10.2172/1765663`

[19] D. Xu, Y. Hao, Y. Luo, C. Montag, and J. Qiang, “Model Parameters Determination in EIC Strong-Strong Simulation”, in *Proc. 5th Int. Particle Accel. Conf. (NAPAC'22)*, Albuquerque, NM, USA, Aug. 2022, pp. 9–11. `doi:10.18429/JACoW-NAPAC2022-MOYD4`

[20] D. Xu *et al.*, “Advancing electron injection dynamics and mitigation approaches in the Electron-Ion Collider’s swap-out injection scheme”, in *Proc. IPAC’24*, Nashville, TN, May 2024, pp. 230-233. doi:10.18429/JACoW-IPAC2024-MOPC72

[21] R. Lindberg, "Note on the Haissinski equilibrium for space charge impedance", Private Communication.

[22] T. Mastoridies, T. Loe, M. Blaskiewicz, "EIC Transverse Instabilities due to the Crab Cavity Fundamental Impedance" *accepted PRAB*

[23] S. Verdú-Andrés, "Electron clouds in the EIC's Hadron Storage Ring and possible mitigations", unpublished (2024). https://brookhavenlab.sharepoint.com/.../EIC-Design-Meeting/

[24] G. Iadarola and G. Rumolo, "PyECLOUD and build-up simulations at CERN. in *Proc. Joint INFN-CERN-EuCARD-AccNet Workshop on Electron-Cloud Effects*, p. 286. 10.5170/CERN-2013-002.189

[25] A. Oeftiger, "An Overview of PyHEADTAIL". CERN-ACC-NOTE-2019-0013 (2019). http://cds-lb.cern.ch/record/2672381/files/CERN-ACC-NOTE-2019-0013.pdf

[26] X. Gu, A. Blednykh, Alexei, M. Blaskiewicz, G. Robert-Demolaize, and S. Verdú-Andrés. "Electron Cloud Simulations for the Electron-Ion Collider in Brookhaven National Laboratory". BNL-224221-2023-TECH; EIC-ADD-TN-053 (2022). https://doi.org/10.2172/1969916

[27] S. Verdú-Andrés. "Electron cloud thresholds at the arcs of the Electron-Ion Collider hadron storage ring". BNL-224588-2023-TECH; EIC-ADD-TN-065 (2023). https://doi.org/10.2172/1992863

[28] S. Verdú-Andrés *et al.*, "RHIC APEX 2024-04: Verification of RHIC Octupoles Dynamic Aperture Limitations - Experimental Plan", unpublished (2024). https://www.c-ad.bnl.gov/APEX/AllPresentation/2024/SchedulesAndPlans/Sep18/APEX_24-4_ExperimentPlan_v3.pdf

[29] S. Verdú-Andrés, J. M. Brennan, M. Blaskiewicz, *et al.*, "A beam screen to prepare the RHIC vacuum chamber for EIC hadron beams: conceptual design and requirements", in *Proc. IPAC’21*, Campinas, SP, Brazil, May 2021, pp. 2066-2068. doi:10.18429/JACoW-IPAC2021-TUPAB260

[30] S. Verdú-Andrés, M. Blaskiewicz, C. Hetzel, V. Ptitsyn, and H. Witte, "Screen magnetic permeability", unpublished (2024). https://brookhavenlab.sharepoint.com/.../EIC-HSR-Vacuum/

[31] D. Xu *et al.*, “Effect of electron orbit ripple on proton emittance growth in EIC”, in *Proc. IPAC’23*, Venice, Italy, May 2023, pp. 108-111. doi:10.18429/JACoW-IPAC2023-MOPA039

[32] D. Xu, “Interplay between beam-beam interaction and noise in EIC” in *ICFA mini workshop: Beam-beam effects in circular colliders*, Lausanne, Switzerland, Sept. 2024.

[33] W. F. Bergan, “Plasma Simulations for an MBEC Cooler for the EIC”, in *Proc. IPAC 2021*, Campinas, SP, Brazil, May 2021, pp. 1823-1826. doi:10.18429/JACoW-IPAC2021-TUPAB180

[34] S. Nagaitsev, “Intrabeam scattering formulas for fast numerical evaluation”, Phys. Rev. ST Accel. Beams 8, 064403 (2005). doi:10.1103/PhysRevSTAB.8.064403

[35] D. Bjorken and S. K. Mtingwa, “Intrabeam scattering”, Part. Accel. vol. 13, pp. 115-143 (1983).

[36] W. F. Bergan *et al.*, “Coherent electron cooling physics for the EIC”, in *Proc. IPAC 2024*, Nashville, TN, USA, May 2024, pp. 1937-2942. doi:10.18429/JACoW-IPAC2024-THYD1

[37] M. A. Furman and M. S. Zisman, “Luminosity”, in *Handbook of Accelerator Physics and Engineering*, 2nd Ed., edited by A. W. Chao, K. H. Mess, M. Tigner, and F. Zimmermann, pp. 311-318 (2013).

[38] P. Baxevanis, "Three-dimensional analysis of microbunched electron cooling", *submitted to Rhys. Rev. ST-AB, Under Review*

[39] M. Blaskiewicz, “Beam-Beam Damping of the Ion Instability”, in *Proc. NAPAC’19*, Lansing, MI, USA, Sep. 2019, pp. 391–394. doi:10.18429/JACoW-NAPAC2019-TUPLM11

[40] D. Xu, M. Blaskiewicz, Y. Luo, D. Marx, C. Montag, and B. Podobedov, “Effect of electron orbit ripple on proton emittance growth in EIC”, in *Proc. IPAC’23*, Venice, Italy, May 2023, pp. 108–111. doi:10.18429/JACoW-IPAC2023-MOPA039

[41] B. Podobedov, H. Witte and M. Blaskiewicz, “Eddy current shielding of the magnetic field ripple in the EIC electron storage ring vacuum chambers”, in *Proc. IPAC’24*, Nashville, TN, May 2024, pp. 246-249. doi:10.18429/JACoW-IPAC2024-MOPC77

[42] B. Podobedov and M. Blaskiewicz, “Transversely driven coherent beam oscillations in the EIC electron storage ring”, in *Proc. IPAC’24*, Nashville, TN, May 2024, pp. 242-245. doi:10.18429/JACoW-IPAC2024-MOPC76

[43] B. Podobedov, M. Blaskiewicz, "Transversely driven coherent beam oscillations and specifications for high-frequency ESR dipole power supply current ripple", EIC-ADD-TN-054, 2024

[44] B. Podobedov, M. Blaskiewicz, Y. Luo, D. Marx, C. Montag, D. Xu, "ESR Dipole Power Supply Current Ripple and Noise Specifications", BNL-224464-2023-TECH, EIC-ADD-TN-059, (2023)

[45] B. W. Montague, "Polarized beams in high energy storage rings", Phys. Rept. 113, pp. 1-96, 1984. doi:10.1016/0370-1573(84)90031-0